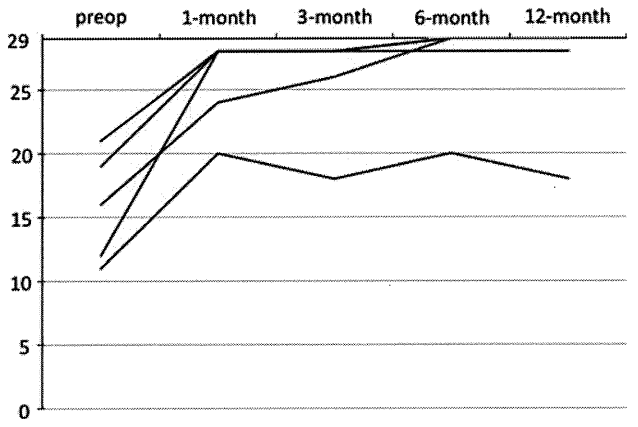

Fig. 4 Sequential changes in the Japan Orthopaedic Association (JOA) score of the five cases. The graph indicates a rapid recovery of the patients' clinical status within 1 month

Radiological results

Dynamic radiological examination showed a solid bony construct without abnormal segmental motion or radiolucency around the implants in all cases after 3 months. No patient exhibited significant implant subsidence during the follow-up period. Immediate postoperative MDCT demonstrated good apposition between the vertebral endplate and implant in all but one case. These findings indicated good anchoring of the porous titanium implant to the surrounding bone. Follow-up MDCT showed good bone ingrown onto the surface of the porous titanium metal without radiolucent line. It also showed remodeling not only of the monitoring bone but also of the surrounding vertebral bone. However, in Case 5, a gap was evident between porous titanium metal and surrounding vertebral endplate on the MDCT image immediately after the operation, because of a poor fit of the device surface with an irregular vertebral endplate. The gap was filled gradually and closed at the final follow-up MDCT (Fig. 5a–c). Because the radiological parameters mentioned above were complete in all cases, bony union was considered to be achieved in all cases by 6 months after the operation. Postoperative MRI scans showed no significant AE such as abnormal fluid collection or apparent change in the Modic sign. In three patients with concomitant spinal canal stenosis, successful neural tissue decompression was also confirmed. The postoperative clinical and radiological results are summarized in Table 3.

Illustrative case (Case 1)

This 54-year-old woman had complained of LBP and intractable bilateral LP for 3 years before surgery. These were refractory to adequate conservative treatment. She also complained of an inability to walk for longer than 10 min, with intermittent claudication. A physical examination demonstrated bilateral dysesthesia on the L5 sensory dermatome. Her preoperative JOA score was 21 points and her self-reported VAS was 10 mm for LBP and 60 mm for LP. X-ray images showed degenerative spondylolisthesis at the L4–5 level with instability (Fig. 6a). Preoperative MR imaging demonstrated severe spinal canal stenosis at the L4–5 level. Transforaminal lumbar interbody fusion and spinal canal decompression using our bioactive titanium was performed. The operating time was 173 min and the estimated intraoperative blood loss was 140 mL. Immediate postoperative coronal imaging using MDCT demonstrated a press fit at the interface between the porous titanium metal and the vertebral endplate (Fig. 6b). Three months after the operation, dynamic X-ray imaging demonstrated no abnormal movement (Fig. 6c). Sagittal imaging using MDCT showed a stable interface without a radiolucent line or any clear zones around the pedicle screws, indicating a successful bony union (Fig. 6d). Postoperative MR imaging showed good neural decompression without any AEs. Her JOA score recovered to 29

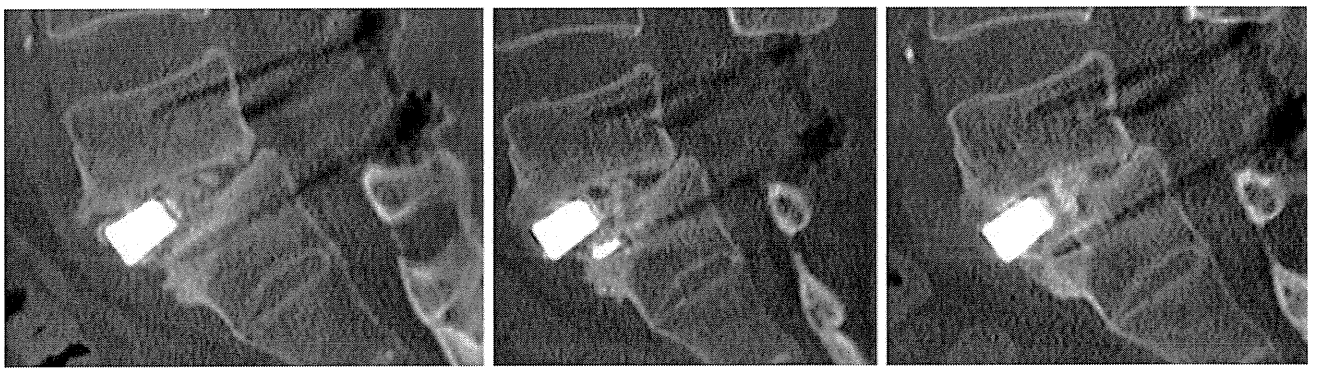

Fig. 5 Sagittal multidetector-row computed tomography (MDCT) images taken immediately postoperatively and at 3 and 12 months for Case 5. The immediate postoperative image (*left*) shows an apparent gap between the porous titanium metal and vertebral bone. The 3-month image (*center*) demonstrates bone ingrowth cranial to the porous titanium metal. The 12-month image (*right*) demonstrates complete gap filling and direct bone bonding to the porous titanium metal

Table 3 Summary of postoperative patient's demographic data

Case	Op. time (min.)	Blood loss (mL)	Post JOA score	JOA score recovery rate (%)	Post VAS (LBP)	Post VAS (LP)	Satisfaction score	ICBG	AEs	Bony union (month)
1	173	140	29	100	0	0	1	–	–	3
2	179	310	29	100	0	0	1	–	–	3
3	160	80	28	90	0	0	1	–	–	3
4	154	228	18	38.9	10	10	4	–	–	6
5	157	192	29	100	0	0	1	–	–	3

ICBG Iliac crest bone graft, *AEs* adverse effects

Satisfaction score 1, very satisfied 2, satisfied 3, somewhat satisfied 4, somewhat dissatisfied 5, dissatisfied

JOA score, VAS, and satisfaction score are obtained at 12 months after the surgery

points and the VAS score was 0 mm for LBP and 0 mm for LP at the final follow-up.

Discussion

Here, we report the safety and efficacy of porous bioactive titanium metal for the treatment of unstable lumbar disc disease. All cases showed early bony union by 6 months without autologous ICBG and rapid recovery after the surgery. The patients' satisfaction and clinical recovery rates were both acceptable.

The use of an interbody fusion cage with autologous bone grafting is a standard procedure for lumbar spinal fusion. However, nonunion, cage subsidence, implant failure and donor site morbidity are still of concern [1]. Porous materials with adequate pore structure and appropriate mechanical properties might represent an alternative to traditional cage implants. Interconnected pores permit tissue ingrowth and thus anchor the prosthesis to the surrounding bone, preventing loosening. This concept also allows a larger support area because no graft space is required and it might be effective for the prevention of implant subsidence. In the current study, significant implant subsidence has not occurred throughout the follow-up periods. Furthermore, if bone bridging can be achieved across the whole implant through the interconnected pores from one vertebra to the other it reduces the risk of implant failure and ensures long-term stability.

The kind of material and its pore characteristics influence the mechanical strength of porous biomaterials. Porous HA implants have good biocompatibility and osteoconductivity, but their mechanical properties are not adequate for load-bearing conditions. The clinical application of such conventional porous materials is limited to non-load-bearing conditions. Therefore, the use of metal to produce porous implants with higher mechanical strength is required. By using titanium metal as a starting material, our device with high porosity and large pore size acquired a high mechanical strength that is adequate for load-bearing conditions. In a previous study, we investigated the relationship between pore structure and bone ingrowth in vivo using several types of porous titanium implants. We concluded that not only high porosity and large pore size but also high interconnectivity of the pores is effective for bone ingrowth and tissue differentiation [23]. Based on this previous study, an optimally structured porous titanium metal was developed and used for this clinical trial. It has 60% porosity, 250 μm average pore size and more than 99% pore interconnectivity.

Another important issue associated with porous metal implants is the difficulty in producing bioactive properties on the inner surfaces of implants using conventional methods such as applying a plasma-sprayed HA coating. In the absence of a bioactive surface, the osteoconductivity of these implants and their capacity to promote fusion is limited. The thickness of a conventional HA coating layer is about 40–50 μm, which cannot be applied to critical supporting structures without changes to surface morphology [5]. Moreover, the conventional HA coating for titanium metal implants has the potential for degradation, absorption and third body wear during long-term implantation, which might be related to its poor clinical results [2, 21]. Our chemical and thermal treatments ensured that bioactive properties were applied to the whole surface of the porous titanium implants without reducing the pore space available for bone ingrowth [15]. Adequate stability of the thin treated layer was confirmed both in vitro and in vivo and might assure the long-term apposition with surrounding bone [9]. This material also offers sufficient resistance to shearing forces during the implantation of treated cementless hip prostheses.

Although titanium metal and its alloys are 'gold standard' materials in orthopedics, one of the potential disadvantages of a metal device is a high elastic modulus. The elastic modulus of solid titanium metal is more than 100 GPa and this will lead to stress shielding around the metal device during long-term implantation. To reduce such a mechanical mismatch between the implant and host

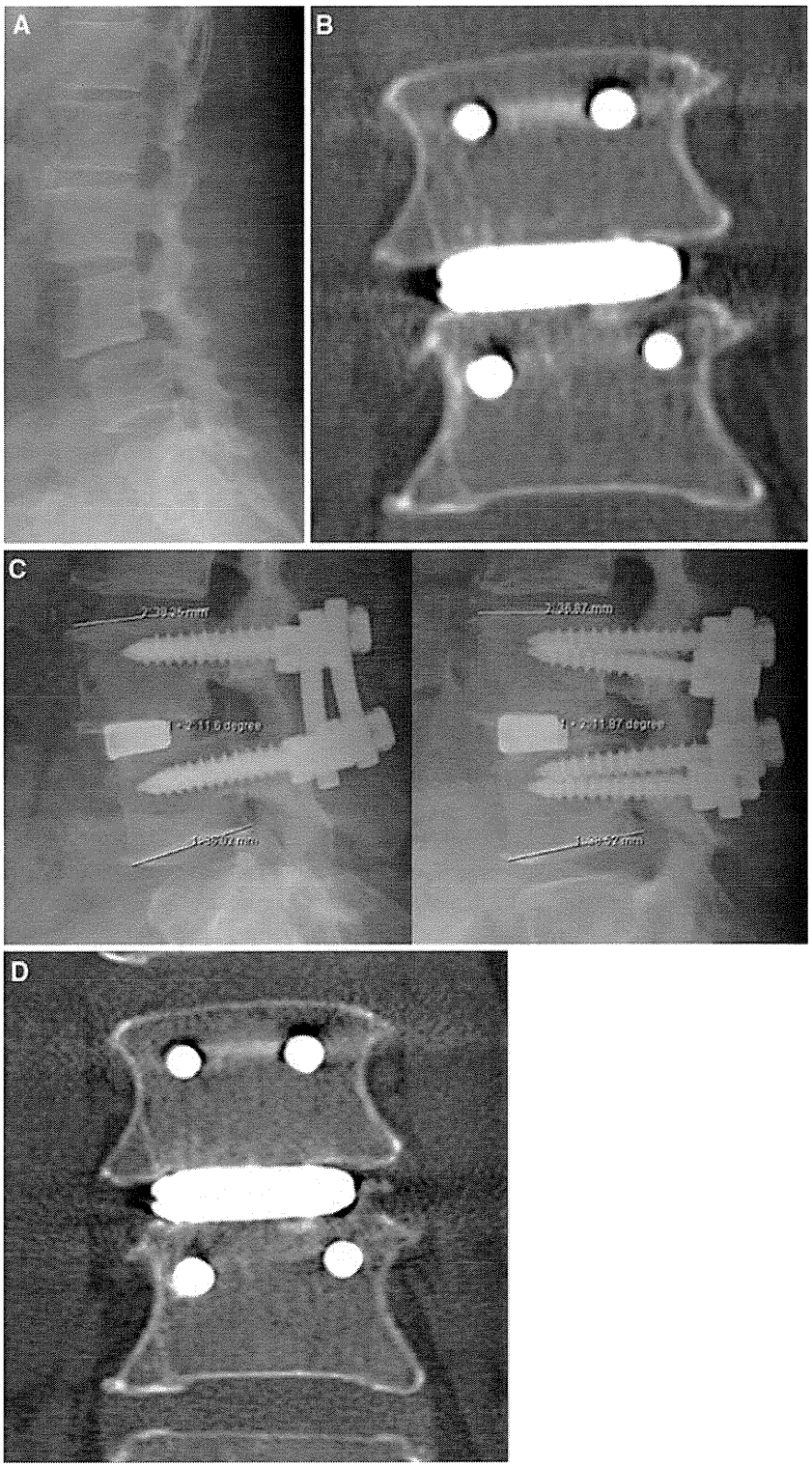

Fig. 6 Preoperative and postoperative radiological studies obtained from a 54-year-old woman with degenerative spondylolisthesis at L4–5 (Case 1). **a** Plain lateral X-ray demonstrating L4 listhesis. **b** Immediate postoperative MDCT image demonstrating a press fit of the porous titanium metal implant to the vertebral endplate. **c** Dynamic lateral radiographs at 3 months showing a solid construct without abnormal segmental motion (*left* flexion; *right* extension). **d** Coronal MDCT image demonstrating solid bony union without device subsidence or any radiolucency at 3 months after surgery

bone, several types of soft material including polyetheretherketone and carbon have been introduced clinically [6, 28]. Although there are no long-term results as yet, porous titanium metal will reduce stress shielding, because the elastic modulus of this material with 60% porosity is 4.2 GPa, close to the value of human cortical bone and much less than solid metal materials. According to Nachemson's study, loads to the human lumbar spine are between 1,000 and 3,000 N during most everyday activities, and increases in different body positions give possible values in excess of 3,000 N during significant lifting [22]. Based upon these data, Brantigan suggested that a lumbar

interbody fusion construct must bear an immediate postoperative load at the bone-implant interface of at least 2,400 N during activities of daily living [4]. On the other hand, breakage of the carbon cage and dissemination of free carbon particles occurred in one case of implant nonunion [29]. A biomechanical study revealed that the carbon cage fractures at around 5,800–8,800 N and concluded that at least 5,000 N was required for an interbody fusion cage [13]. The fatigue strength of porous titanium metal combined with an outer frame is more than 10,000 N under a repetitive compressive load, so it can be used as a spinal interbody fusion device safely.

Another potential disadvantage of a pure metal device is the difficulty of confirming fusion status radiologically because of its high radiodensity. Usually, bony union is confirmed when the following radiological parameters are complete: visible continuous grafted bone trabeculation, no abnormal movement on dynamic study and no radiolucency around the implants. In the case of metal devices such as a titanium cage, bone trabeculation through the cage is difficult to identify on plain X-ray images. However, definitive diagnoses of bony union have become easier with the introduction of MDCT, especially in the case of porous titanium metal, because the metal content is less than with the solid form, recognition of fusion status such as bone-implant interface and bony trabeculation around the implant is not so difficult on MDCT images. In the current study, two specific radiological findings were evident. The first of these was the anchoring effect between the porous bioactive titanium implant and the surrounding vertebral endplate seen on the images taken immediately after surgery. This could be attributed to the optimally rough surface of the porous bioactive device. The second finding was the gap-filling effect. The radiological evidence of gap filling as shown in Fig. 6 resembles the results of alkali- and heat-treated total hip prostheses. Radiological gaps between alkali- and heat-treated metal shells and the acetabulum were filled within 1 year, which indicated the high osteoconductive ability of bioactive titanium metal [14]. The best feature of porous bioactive titanium metal is that it permits bone ingrowth through the inner pore structure. Although we reported good bone ingrowth to the pores in several studies using animal models, we could not confirm this evidence using noninvasive radiological examinations in the present study.

There are some limitations to this study, including its small sample size, short follow-up period and preliminary nature. Our chemical and thermal treatment has been applied clinically for cementless total hip prostheses after a strict clinical trial, which was approved by the Ministry of Health, Labor and Welfare in Japan. Excellent mid-term (4.8 years) clinical results and early bone apposition were reported [14]. These results are encouraging for the efficacy and safety of this surface treatment on titanium and its alloys. Moreover, TLIF is a promising standard procedure for the treatment of patients with unstable spinal disease. Given these encouraging results, we planned this small clinical trial as much as possible to test the efficacy and safety of porous bioactive titanium metal in a spinal fusion device. Fortunately, there was successful bony union without the need for autologous ICBG in this small series. However, implantation of metal devices has a potency to bring about several late complications such as stress shielding and adjacent segment disease during long-term implantation. Therefore, long-term clinical results are mandatory to reveal the true efficacy and safety of this device.

We consider that porous bioactive titanium metal is superior to other porous metal materials in terms of safety, osteoconductive and osteoinductive abilities, mechanical strength and controllable optimum microstructure [10, 24]. Another advantage of porous bioactive titanium metal is its potency for general purpose medical devices. First, our surface treatment can be applied not only to pure titanium but also to several types of titanium alloys. By changing materials, the mechanical characteristics can be optimized. Second, using our manufacturing technique, the pore structure, mechanical strength and biological characteristics can be controlled depending on the conditions. This material will be valuable not only for spinal fusion but also for reconstructive surgery to the skull, the maxillofacial region and in other orthopedic fields. Moreover, adjustments to the elastic modulus and bioactive abilities promise to produce new generations of devices for the treatment of osteoporotic bone.

Conclusions

We developed porous bioactive titanium device for spinal fusion. The optimal mechanical strength and interconnected structure of porous titanium metal were adjusted to the device. The whole surface of porous titanium was treated chemically and thermally to form the bioactive surface. Clinical trial was successfully performed and early bony union was achieved in all cases without ICBG by 6 months. Two specific findings including an anchoring effect and gap filling were evident radiologically. Although a larger and longer-term follow-up clinical study is mandatory to reach any firm conclusions, we consider this porous bioactive titanium metal is promising material for a spinal fusion device.

Acknowledgments The authors thank Hisashi Kitagaki, Tsuneo Teraoka, of Osaka Yakin Co., for manufacturing and providing the porous titanium implants. They thank Seiji Yamaguchi, of Chubu University Biomedical Sciences, for treating the material chemically.

They thank Shuji Higuchi, Masanori Fukushima, Satoshi Teramukai, Kenichi Yoshimura, Toshinori Murayama, Tomoko Yokota, Erika Hirata and Harue Tada, of Kyoto University's translational research center, for help in protocol preparation, moderation of the clinical trial and data management. They also thank Takeshi Sakamoto, Makoto Yoshida and Masahiko Miyata for radiological assessments, and Masato Ota for surgical assistance.

This study was supported by a Grant in Aid for Scientific Research from the Japan Society for the Promotion of Science (No. 19200039). No benefits in any form have been or will be received from a commercial party related directly or indirectly to the subject of this manuscript. This manuscript has not been previously published and is not under consideration for publication elsewhere. The first two authors contributed equally to this study and preparation of this manuscript.

References

1. Banwart JC, Asher MA, Hassanein RS (1995) Iliac crest bone graft harvest donor site morbidity. A statistical evaluation. Spine 20:1055–1060
2. Bloebaum RD, Beeks D, Dorr LD, Savory CG, DuPont J, Hofmann AA (1994) Complications with hydroxyapatite particulate separation in total hip arthroplasty. Clin Orthop 298:19–26
3. Boden SD, Zdeblick TA, Sandu HS, Heim SE (2000) The use of rhBMP-2 in interbody fusion cages: definitive evidence of osteoinduction in humans: a preliminary report. Spine 25:376–381
4. Brantigan JW, Cunningham BW, Warden K, McAfee PC, Steffee AD (1993) Compression strength of donor bone for posterior lumbar interbody fusion. Spine 18:1213–1221
5. De Groot K, Geesink R, Klein CP, Serekian P (1987) Plasma sprayed coatings of hydroxyapatite. J Biomed Mater Res 21: 1375–1381
6. Desogus N, Ennas F, Leuze R et al (2005) Posterior lumbar interbody fusion with PEEK cages: personal experience with 20 patients. J Neurosurg Sci 49:137–141
7. Ducheyne P, Qiu Q (1999) Bioactive ceramics: the effect of surface reactivity on bone formation and bone cell function. Biomaterials 20:2287–2303
8. Fujibayashi S, Shikata J, Tanaka C, Matsushita M, Nakamura T (2001) Lumbar posterolateral fusion with biphasic calcium phosphate ceramic. J Spinal Disord 14:214–221
9. Fujibayashi S, Nakamura T, Nishiguchi S, Tamura J, Uchida M, Kim HM et al (2001) Bioactive titanium: effect of sodium removal on the bone-bonding ability of bioactive titanium prepared by alkali and heat treatment. J Biomed Mater Res 56:562–570
10. Fujibayashi S, Neo M, Kim HM, Kokubo T, Nakamura T (2004) Osteoinduction of porous bioactive titanium metal. Biomaterials 25:443–450
11. Fujibayashi S, Neo M, Takemoto M, Ota M, Nakamura T (2010) Paraspinal-approach transforaminal lumbar interbody fusion for the treatment of lumbar foraminal stenosis. J Neurosurg Spine 13:500–508
12. Hench LL (1998) Bioactive materials: the potential for tissue regeneration. J Biomed Mater Res 41:511–518
13. Jost B, Cripton PA, Lund T, Oxland TR, Lippuner K, Jaeger P et al (1998) Compressive strength of interbody cages in lumbar spine: the effect of cage shape, posterior instrumentation and bone density. Eur Spine J 7:132–141
14. Kawanabe K, Ise K, Goto K, Akiyama H, Nakamura T, Kaneuji A et al (2009) A new cementless total hip arthroplasty with bioactive titanium porous-coating by alkaline and heat treatment: average 4.8-year results. J Biomed Mater Res Part B: Appl Biomater 90B:476–481
15. Kim HM, Kokubo T, Fujibayashi S, Nishiguchi S, Nakamura T (2000) Bioactive macroporous titanium surface layer on titanium substrate. J Biomed Mater Res 52:553–557
16. Kokubo T (1991) Bioactive glass ceramics: properties and applications. Biomaterials 12:155–163
17. Kokubo T, Kushitani H, Sakka S, Kitsugi T, Yamamuro T (1990) Solutions able to reproduce in vivo surface-structure changes in bioactive glass-ceramic A-W. J Biomed Mater Res 24:721–734
18. Kokubo T, Miyaji F, Kim HM, Nakamura T (1996) Spontaneous formation of bonelike apatite layer on chemically treated titanium metals. J Am Ceram Soc 79:1127–1129
19. McClellan JW, Mulconrey DS, Forbes RJ, Fullmer N (2006) Vertebral bone resorption after transforaminal lumbar interbody fusion with bone morphogenetic protein (rhBMP-2). J Spinal Disord Tech 19:483–486
20. Modic MT, Steinberg PM, Ross JS, Masaryk TJ, Carter JR (1988) Degenerative disk disease: assessment of changes in vertebral body marrow with MR imaging. Radiology 166:193–199
21. Morscher EW, Hefti A, Aebi U (1998) Severe osteolysis after third body wear due to hydroxyapatite particles from acetabular cup coating. J Bone Joint Surg Br 80:267–272
22. Nachemson AL (1981) Disc pressure measurements. Spine 6:93–97
23. Otsuki B, Takemoto M, Fujibayashi S, Neo M, Kokubo T, Nakamura T (2006) Pore throat size and connectivity determine bone and tissue ingrowth into porous implants: three-dimensional micro-CT based structural analyses of porous bioactive titanium implants. Biomaterials 27:5892–5900
24. Takemoto M, Fujibayashi S, Neo M, Suzuki J, Kokubo T, Nakamura T (2005) Mechanical properties and osteoconductivity of porous bioactive titanium. Biomaterials 26:6014–6023
25. Takemoto M, Fujibayashi S, Neo M, Suzuki J, Matsushita T, Kokubo T, Nakamura T (2006) Osteoinductive porous titanium implants: effect of sodium removal by dilute HCl treatment. Biomaterials 27:2682–2691
26. Takemoto M, Fujibayashi S, Neo M, So K, Akiyama N, Matsushita T et al (2007) A porous bioactive titanium implant for spinal interbody fusion: an experimental study using a canine model. J Neurosurg Spine 7:435–443
27. Toth JM, Boden SD, Burkus JK MD, Badura JM, Peckham SM, McKay WF (2009) Short-term osteoclastic activity induced by locally high concentrations of recombinant human bone morphogenetic protein-2 in a cancellous bone environment. Spine 34:539–550
28. Tullberg T, Brandt B, Rydberg J, Fritzell P (1996) Fusion rate after posterior lumbar interbody fusion with carbon fiber implant: 1-year follow-up of 51 patients. Eur Spine J 5:178–182
29. Tullberg T (1998) Failure of a carbon fiber implant: a case report. Spine 23:1804–1806
30. Vaccaro AR, Lawrence JP, Patel T, Katz LD, Anderson DG, Fischgrund JS et al (2008) The safety and efficacy of OP-1 (rhBMP-7) as a replacement for iliac crest autograft in posterolateral lumbar arthrodesis. Spine 33:2850–2862
31. Vaidya R, Sethi A, Bartol S, Jacobson M, Coe C, Craig JG (2008) Complications in the use of rhBMP-2 in PEEK cages for interbody spinal fusions. J Spinal Disord Tech 21:557–562
32. Wen CE, Mabuchi M, Yamada Y, Shimojima K, Chino Y, Asahina T (2001) Processing of biocompatible porous Ti and Mg. Scripta Mater 45:1147–1153

Acta Biomaterialia 7 (2011) 2327–2336

Contents lists available at ScienceDirect

Acta Biomaterialia

journal homepage: www.elsevier.com/locate/actabiomat

Osteoinduction of porous Ti implants with a channel structure fabricated by selective laser melting

A. Fukuda [a,*], M. Takemoto [a], T. Saito [a], S. Fujibayashi [a], M. Neo [a], Deepak K. Pattanayak [b], T. Matsushita [b], K. Sasaki [c], N. Nishida [c], T. Kokubo [b], T. Nakamura [a]

[a] Department of Orthopaedic Surgery, Graduate School of Medicine, Kyoto University, Shogoin, Kawahara-cho 54, Sakyo-ku, Kyoto 606-8507, Japan
[b] Department of Biomedical Sciences, College of Life and Health Sciences, Chubu University, 1200 Matsumoto-cho, Kasugai, Aichi 487-8501, Japan
[c] Sagawa Printing Co. Ltd., 5-3 Inui, Morimoto-cho, Mukou, Kyoto 617-8581, Japan

ARTICLE INFO

Article history:
Received 14 September 2010
Received in revised form 22 January 2011
Accepted 27 January 2011
Available online 2 February 2011

Keywords:
Osteoinduction
Interconnective pore size
Channel structure
Bioactive titanium
Selective laser melting

ABSTRACT

Many studies have shown that certain biomaterials with specific porous structures can induce bone formation in non-osseous sites without the need for osteoinductive biomolecules, however, the mechanisms responsible for this phenomenon (intrinsic osteoinduction of biomaterials) remain unclear. In particular, to our knowledge the type of pore structure suitable for osteoinduction has not been reported in detail. In the present study we investigated the effects of interconnective pore size on osteoinductivity and the bone formation processes during osteoinduction. Selective laser melting was employed to fabricate porous Ti implants (diameter 3.3 mm, length 15 mm) with a channel structure comprising four longitudinal square channels, representing pores, of different diagonal widths, 500, 600, 900, and 1200 μm (termed p500, p600, p900, and p1200, respectively). These were then subjected to chemical and heat treatments to induce bioactivity. Significant osteoinduction was observed in p500 and p600, with the highest observed osteoinduction occurring at 5 mm from the end of the implants. A distance of 5 mm probably provides a favorable balance between blood circulation and fluid movement. Thus, the simple architecture of the implants allowed effective investigation of the influence of the interconnective pore size on osteoinduction, as well as the relationship between bone quantity and its location for different pore sizes.

1. Introduction

Bioactive materials such as bioglass, hydroxyapatite (HA), other calcium phosphate-based biomaterials, and A–W glass ceramic can directly bond to living bones [1] via an apatite layer. Furthermore, when these bioactive materials have a specific porous structure they sometimes become osteoinductive within soft tissues even without the addition of osteogenic cells or bone morphogenetic protein [2–9]. We have previously shown that even porous Ti containing no calcium phosphate can become osteoinductive when it has a complex interconnecting porous structure and bioactive surfaces activated by simple chemical and thermal treatments [10]. In these studies we found that complex macroporous structures, microrough surfaces, and apatite-forming abilities are prerequisites for osteoinduction. Modification of the physico-chemical or surface properties appears to be an attractive method for improving the osteogenic capacity of synthetic materials. Although the clinical utility of osteoinductivity in biomaterials remains controversial, some reports have suggested that this property is a distinct advantage for biomaterials intended for use as bone substitutes [11–14]. Therefore, we believe that it is important in the development of porous biomaterials to tailor osteoinductivity to the specific purpose.

For macroporous structures in general it is recognized that well-defined concavities are important. However, the most suitable pore structure has not been clearly identified. In previous studies we employed plasma sprayed or powder sintered porous bioactive Ti in order to investigate the influence of different porous structures on osteoinduction [10,15]. However, the conventional manufacturing methods employed in our previous studies did not allow precise control over porosity, pore size, and interconnectivity. Furthermore, other osteoinductive materials, such as porous biphasic calcium phosphate [16,17] and porous β-tricalcium phosphate [18,19], are unsuitable for the investigation of macroporous structures because their pore structures change over the implantation period.

Since the 1980s rapid prototyping (RP) technology has emerged as a revolutionary manufacturing process with inherent capabilities for the rapid fabrication of objects of virtually any shape. Using this technology it has become possible to automatically generate three-dimensional (3D) objects by combining computer-aided

* Corresponding author. Tel.: +81 75 751 3365; fax: +81 75 751 8409.
E-mail address: akinobu@kuhp.kyoto-u.ac.jp (A. Fukuda).

1742-7061/$ - see front matter © 2011 Acta Materialia Inc. Published by Elsevier Ltd. All rights reserved.
doi:10.1016/j.actbio.2011.01.037

design (CAD) data and computer-aided manufacturing (CAM), and such objects have been used to fabricate scaffolds or orthopedic implants [20–22]. Furthermore, when Ti is used in RP to produce biomaterials it must be non-resorbable and structurally invariant for accurate evaluation of the pore structure. Among the several RP techniques available we adopted the selective laser melting (SLM) [20–22] process, because it is compatible with Ti and can be used to control the configurations directly with dimensional accuracies of the order of several hundred micrometers. SLM is a powder-based additive manufacturing technique that is capable of producing parts in a layer by layer fashion from a 3D CAD model by employing a high energy laser beam that fuses the metal powders present in its focal zone. SLM is now considered a promising fabrication technique, and we intend to apply it to orthopedic implants under load-bearing conditions.

SLM allows the manufacture of implants with an irregular structure that mimics that of human cancellous bone, which thus far had not been possible with commercially pure Ti (cp-Ti). We reported the tensile strength, surface structure, and apatite forming ability of such devices after chemical and thermal treatment [23]. Furthermore, in our preliminary study these cancellous bone mimicking Ti implants were found to be effective bone substitutes in vivo because of the osteoconductivity and osteoinductivity induced by our chemical and thermal treatments.

In the present study, we evaluated the effects of the interconnective pore size on osteoinductivity (speed, amount, and location of bone formation) to establish basic data for developing a porous osteoinductive biomaterial. At the same time we expect to acquire new knowledge about the mechanisms behind osteoinduction.

For this purpose we used SLM to manufacture porous Ti implants, referred to as channel implants, each with four square longitudinal channels, representing interconnected pores, of different diagonal widths, 500, 600, 900, and 1200 μm. This pore design allowed a comparison of osteoinductivity for different pore sizes in identical environments. These implants were subsequently chemically and thermally treated to induce bioactivity [12] and then implanted into the back muscles of mature beagle dogs.

2. Materials and methods

2.1. Materials

Cylindrical channel implants (diameter 3.3 mm, length 15 mm) were designed using a CAD program (Magics®, Materialise, Belgium) (Fig. 1A) and the design data stored in STL file format, commonly used in stereolithography. All the cylinders had four longitudinal square channels, acting as pores, of different diagonal widths, 500, 600, 900, and 1200 μm. In the present paper these cylinders are referred to as p500, p600, p900, and p1200, respectively. As outlined above, we set this range of target channel sizes on the basis of the fact that an SLM machine can only efficiently produce features larger than 500 μm across and the reported upper limit for osteoconduction is around 1000 μm [24–27]. The STL data were converted into slice data that defined the path for the laser scan inside the cross-sectional contours of the produced shapes. The channel implants were fabricated by an EOSINT M270 SLM machine (Electro Optical Systems GmbH, Germany) using cp-Ti powder (>99.5% pure) with particle diameters of less than 45 μm (Osaka Titanium Technologies, Japan).

2.2. Manufacturing porous Ti implants

After the slice data had been obtained the porous Ti powder was melted using an Yb fiber laser beam in an argon gas atmosphere and then the selected slice of the product was solidified. Then the top of the previously melted surface was recoated with a layer (thickness 30 μm) of fresh Ti powder using a recoater blade. Subsequently, selective irradiation was again carried out using the laser beam. These steps were repeated and as the layers were stacked on top of each other the final geometry was achieved. The process

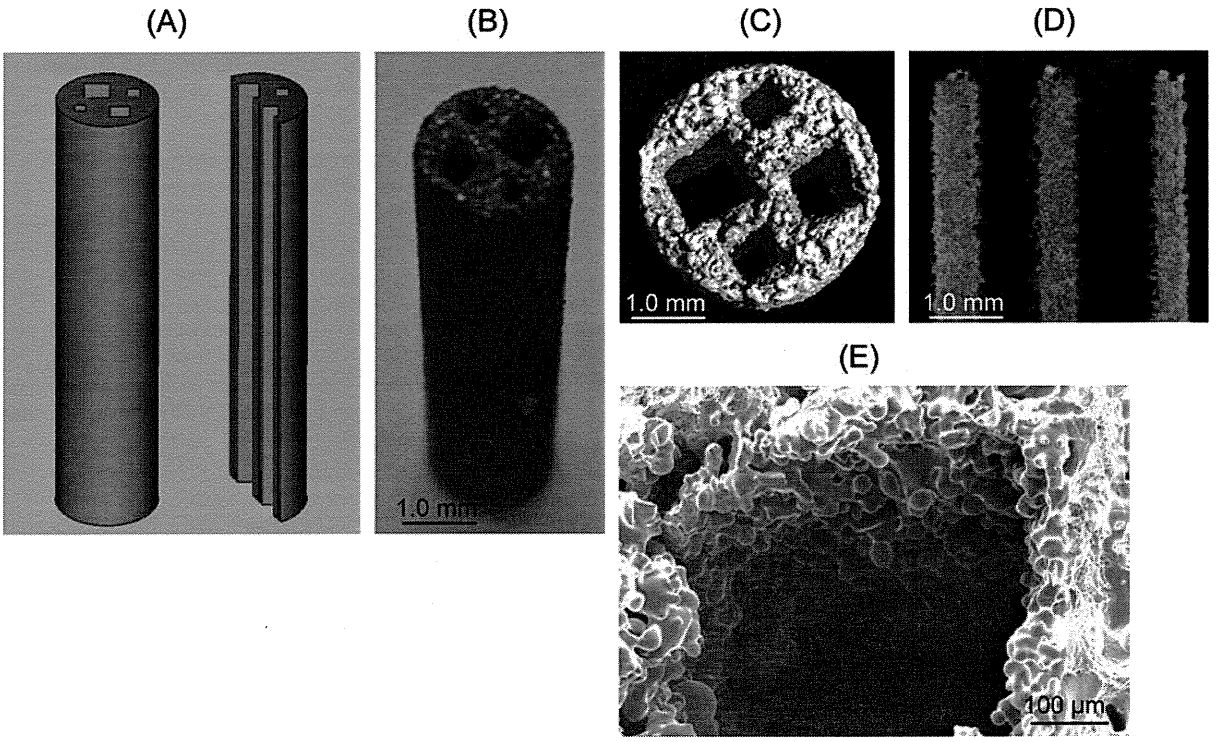

Fig. 1. (A) Computer-aided design (CAD) of a channel implant with four square channels (diagonal widths 500, 600, 900, and 1200 μm). (B) Manufactured channel implant. (C, D) Microcomputed tomography (μCT) of the rapid prototyped channel implant. (E) SEM image of a cross-section of after heat treatment at 1300 °C. Microporous structure was observed on the surface of the smallest of the four pores (500 μm).

parameters for the SLM method were optimized to suppress distortion during the layered fabrication process [28] and were as follows: laser power 117 W, scanning speed 225 mm s^{-1}, hatch spacing 90 μm, hatch offset 20 μm. After the SLM process the channel implants were heat treated at 1300 °C for 1 h and allowed to naturally cool in the furnace under an argon gas atmosphere to enhance ductility and to introduce small cavities on the walls of the channels (Fig. 1B).

2.3. Assessment of manufactured implant structure

About 10 samples were fabricated and the sizes of their various parts measured. Three slices were chosen randomly from each sample and were accurately measured by high resolution X-ray microcomputed tomography (micro-CT) (SMX-100CT-SV3, Shimadzu Co., Japan). The values obtained were averaged. The average values of the outer diameter and shaft length of the implants and the diagonal width of each channel were compared with the design values. The channel implants were also examined under a scanning electron microscope (S-4700, Hitachi Ltd., Japan).

2.4. Induction of bioactivity

The channel implants were soaked in 5.0 M aqueous NaOH at 60 °C for 24 h and then in 0.5 mM HCl (pH 3.4) at 40 °C for 24 h, gently washed with distilled water, and dried at 40 °C for 24 h at room temperature [12]. During these solution treatments the samples were inserted into a polypropylene tube with an inner diameter of 3.6 mm and the solutions were forced into the channels and over the outside surface using a pump. These implants were subsequently heated to 600 °C in an electric furnace at a heating rate of 5 °C min^{-1}, maintained at 600 °C for 1 h, and then allowed to cool to room temperature. Untreated implants were used as control samples.

2.5. Assessment of in vitro apatite forming ability of channel implants

The in vitro apatite forming ability of the channel implants was examined using a simulated body fluid (SBF) having a pH of 7.40 and the ion concentrations (mmol l^{-1}): Na^+ 142.0, K^+ 5.0, Ca^{2+} 2.5, Mg^{2+} 1.5, Cl^- 147.8, HCO_3^- 4.2, HPO_4^{2-} 1.0, SO_4^{2-} 0.5 [29,30]. The channel implants remained in SBF for 3–7 days at 36.5 °C under the reflux conditions mentioned in Section 2.4, then were removed from the SBF, washed with distilled water, and dried on a clean bench. The surface of the samples was examined by field emission scanning electron microscopy (FE-SEM) (S-4300, Hitachi, Japan), and any apatite formed was identified by thin film X-ray diffractometry (TF-XRD) (RINT-2500, Rigaku Co., Japan).

2.6. Animal study

The channel implants were conventionally sterilized using ethylene oxide gas and then implanted in the dorsal muscles of eight mature beagle dogs (weight 10–11 kg), for periods of 16, 26, or 52 weeks. The animals were anesthetized by intramuscular administration of ketamine hydrochloride (50 mg kg^{-1}), followed by diazepam (5 mg) and atropine sulfate (0.5 mg), without endotracheal intubation. Just before the operation a dose of 10 mg kg^{-1} pentobarbital sodium was injected intravenously. During the operation the dogs received an intravenous infusion of saline containing isepamicin sulfate antibiotic. The operations were performed under standard sterile conditions. After incising the skin and fascia, muscle pouches were carefully made in the dorsal muscle to limit any bleeding. Three treated implants and three untreated implants were inserted on both the right and left sides of the dorsal muscles. Each pouch was marked with 3-0 nylon sutures to facilitate explantation. Two implants each were removed from the eight animals under the anesthesia mentioned above at 16, 26, and 52 weeks.

This animal study was approved by the Animal Research Committee, Graduate School of Medicine, Kyoto University, Japan.

2.7. Histological examination

Following killing the implant sites were removed and prepared for histological examination. The specimens were fixed in 10% phosphate-buffered formalin with a pH of 7.25 for 7 days and dehydrated in serial concentrations of ethanol (70, 80, 90, 99, 100, and 100 vol.%) for 3 days each. The specimens were then embedded in polyester resin and cut with a band saw (BS-3000CP, EXACT cutting system, Norderstedt, Germany) perpendicular to the longitudinal axis of the implant from both ends to the mid portion at 1 mm intervals. The sliced samples were ground at their ends to a thickness of 60–70 μm using a grinding–sliding machine (microgrinding MG-4000, EXACT) in order to clarify the distance from the ends of the implants (Fig. 2A). As a result, the mid portion of the channel implants was in the seventh slice, as the total number of slices was 14. For staining we used the method of Maniatopoulos et al. [31], who reported that cells and extracellular structures are stained blue with Stevenel's blue and bone is stained orange or purple with Van Gieson's picrofuchsin. An in-depth microscopic analysis was performed on the histological slides using transmitted light microscopy (Nikon Model Eclipse 80i) in conjunction with a digital camera (Nikon DS-5M-L1).

Several sections were ground with diamond paper until the staining had been removed and a thin layer of carbon was applied for observation by backscattered SEM and SEM energy dispersive X-ray microanalysis (SEM-EDX).

2.8. Histomorphometric examination

Bone formation in each channel was evaluated by light and fluorescence microscopy. The percent bone formation length (PBFL), which is the percentage of slices with bone from among the total 14 slices per implant in each channel, was evaluated for each implantation time (Fig. 2B).

The percent bone formation area (PBFA), which is the percentage of channel area covered with bone in each channel at each distance along the channel, was measured on a personal computer using Adobe Photoshop CS3 and Image J (NIH). The cumulative total bone formation area (i.e. PBFA × channel area, in mm^2) on each slice for each channel was defined as the total induced bone volume (TIBV) (mm^3). We then averaged the PBFA of each slice for each channel (Fig. 2C). Finally, the locations where osteoinduction occurred in each channel were identified. These locations were represented as a line graph of PBFA of each channel at the respective distance from the near end.

2.9. Statistical analysis

Four different channel widths (p500, p600, p900, and p1200) were analyzed for each implantation period (16, 26, and 52 weeks post-implantation). Data was recorded as the mean ± standard deviation (SD) and assessed using one-way analysis of variance (ANOVA) followed by Tukey–Kramer multiple comparison post hoc tests. Differences of $P < 0.05$ were considered to be statistically significant.

3. Results

3.1. In vitro evaluation

3.1.1. Manufacture and characterization of rapid prototyped channel implants

The measured values from the micro-CT images (Fig. 1C and D) for the 10 samples are averaged and summarized in Table 1. The

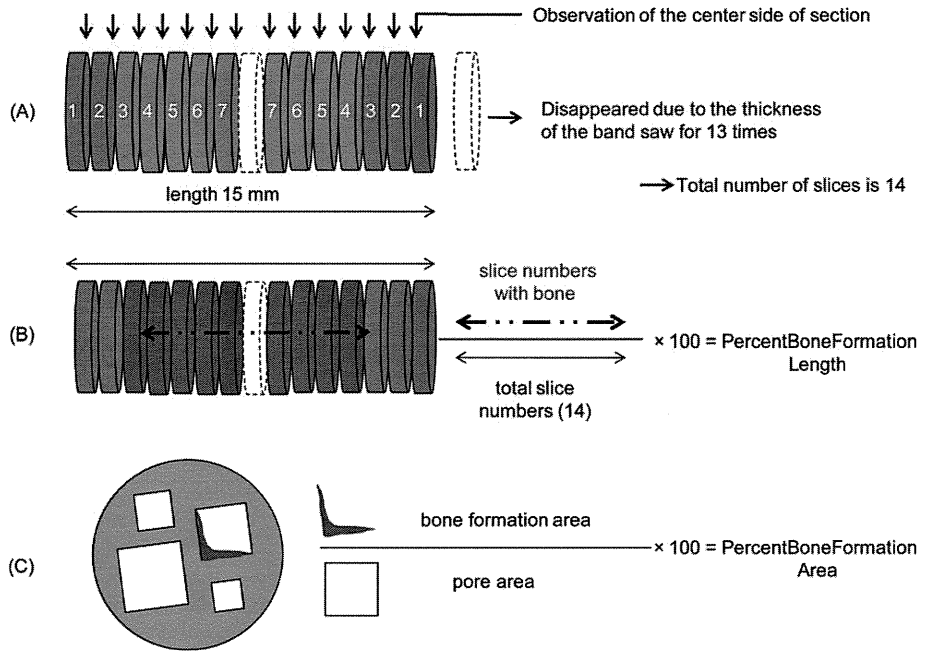

Fig. 2. Schema of the assessment procedure. (A) Detailed method for preparing the 1 mm slice section. (B) Percent bone formation length was calculated as the percentage of slices with bone from among the total 14 slices. Red slices indicate slices with osteoinduction. (C) Percent bone formation area is the percentage of pore area covered in new bone.

Table 1
Comparison of the design and measured dimensions of 10 samples fabricated by selective laser melting.

	Diameter (mm)	Height (mm)	Diagonal length (μm)			
Design value	3.3	15	500	600	900	1200
Measured value	3.20 ± 0.077	15.05 ± 0.2	523.67 ± 36.82	636.87 ± 27.27	947.63 ± 43.88	1264.73 ± 23.42

actual diagonal widths were 524 ± 37, 637 ± 27, 948 ± 44, and 1265 ± 23 μm for p500, p600, p900, and p1200, respectively. The percentage errors were 4.73%, 6.14%, 5.29%, and 5.39%, respectively – 3.03% for an outer diameter of 3.3 mm and 0.31% for a shaft length of 15 mm.

Fig. 1C and D shows micro-CT images of a channel implant fabricated by SLM. The dimensions and internal structure have been faithfully reproduced in accordance with the CAD design. In addition, the external and internal surfaces were observed to form rough structures, such as rugae, on heat treatment at 1300 °C after the SLM treatment. Fig. 1E shows SEM images of a p500 implant which had been divided into two using pliers. The rough structure has the appearance of rugae with a uniform microporous structure on each channel surface.

3.1.2. Surface morphology before implantation

The SEM figures showed that the channel wall surfaces of the untreated channel implants were smooth (Fig. 3A). In contrast, a fine nanosized network structure was observed on the outer surface and on every channel wall surface of the central portion (Fig. 3B and C) of the treated samples. In this manner the SEM figures revealed that in the bioactive channel implants the chemical and thermal treatments successfully penetrated the implant core.

3.1.3. Assessment of in vitro apatite forming ability

After the divided channel implants had been soaked in SBF apatite particles were deposited over the entire surface within 3 days in every channel (Fig. 3D); this indicates that the channel implants possess a homogeneous bioactive surface layer throughout the inner channels of the implant. On the other hand, no surface morphological changes or apatite deposits were observed in the untreated channel implants after soaking in SBF for 7 days.

3.2. In vivo evaluation

3.2.1. Gross inspection

All the dogs tolerated the operation well. No infections at the operative site or implant dislocations were observed in the operative field. All the implants were stable at all post-implantation time points. No apparent adverse reactions such as inflammation or foreign body reactions were noted on or around any of the implants.

3.2.2. Histological findings

Within 16 weeks osteoinduction was observed in all the channels of all treated implants. New bone formed as excellent laminated bone along the channel wall surface. Considerably more bone quantity was observed in p500 and p600 than in p900 and p1200. No bone formation could be recognized on the outer surfaces of the bioactive, treated implants, and no crystal formation or pathological calcification was observed. There was no sign of cartilage formation or endochondral ossification. In contrast, no bone formation was detected in any of the untreated implants at all post-implantation times. They were filled with fibrous tissue containing capillaries.

At 26 and 52 weeks (Fig. 4) new bone was observed as more thickly laminated bone along the channel wall surface than at 16 weeks. Hence, the amount of new bone formation clearly increased with time. In a magnified section (Fig. 5) obvious bone

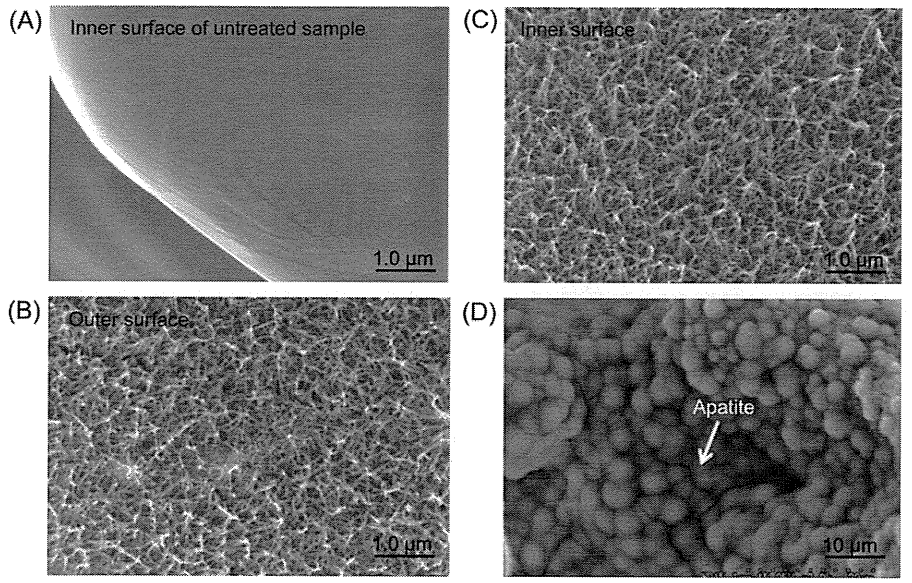

Fig. 3. (A–C) FE-SEM pictures of the outer and inner surface of implant p500. (A) Inner surface of an untreated p500 implant. (B) Outer surface and (C) inner surface of a treated p500 implant. (D) FE-SEM photographs of the surfaces of a treated p500 implant after immersion in SBF for 3 days. Apatite formation on the surface can be seen.

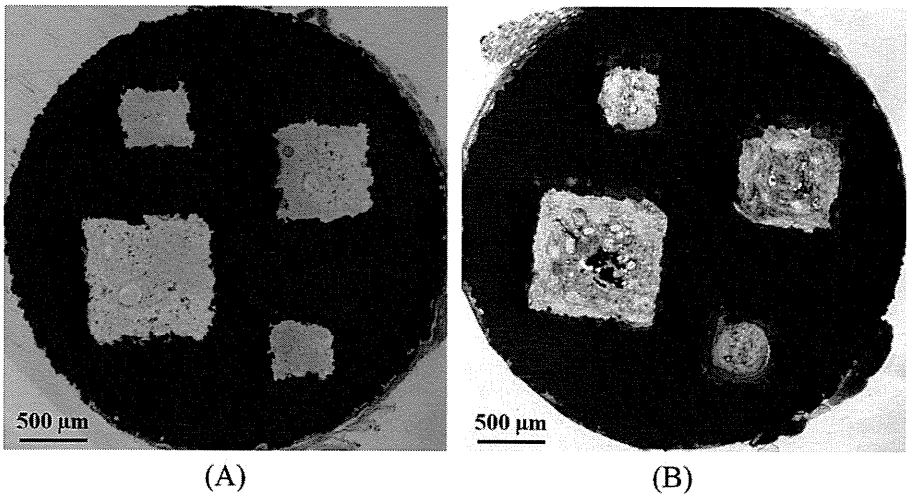

Fig. 4. Non-decalcified histological sections 5 mm from the near end of the untreated and bioactive treated implants at 26 weeks observed by transmitted light microscopy. (A) No bone formation was detected in any untreated implants. (B) Induction of new bone was observed in all pores of treated implants. Stevenel's blue and Van Gieson's picrofuchsin staining. Red color denotes bone.

formation with osteocytes containing blue stained nuclei lined with cuboidal osteoblast-like cells can be seen.

New bone formed on the implant channel surface and bonded directly, as seen in the backscattered SEM image (Fig. 6A). Bony structure (lamella bone with osteocytes) was clearly observed in the backscattered SEM scan. EDX analysis indicated that this bony tissue included calcium and phosphorous with a Ca/P ratio of 1.67 wt.%.

3.2.3. Bone formation length (Fig. 7)

At 16, 26, and 52 weeks the PBFL values for the bioactive implants were 52 ± 12, 54 ± 12, 35 ± 15, and 29 ± 18, 66 ± 8.6, 69 ± 18, 45 ± 20, and 46 ± 17, and 81 ± 14, 74 ± 9, 68 ± 11, and 65 ± 17, respectively, for p500, p600, p900, and p1200, respectively. Furthermore, in the relatively early post-implantation period the PBFL was significantly greater in p500 and p600 than in p900 and p1200. The PBFL for the untreated implants was 0 from 16 to 52 weeks because no bone was observed in any channel.

3.2.4. Total induced bone volume (Fig. 8)

At 16, 26, and 52 weeks the TIBV values for the bioactive implants were 0.17 ± 0.13, 0.26 ± 0.14, 0.23 ± 0.14, and 0.21 ± 0.16, 0.37 ± 0.21, 0.44 ± 0.28, 0.33 ± 0.30, and 0.45 ± 0.43, and 0.51 ± 0.26, 0.57 ± 0.30, 0.80 ± 0.60, and 0.92 ± 0.84, respectively, for p500, p600, p900, and p1200, respectively. As the channel size increased the TIBV increased at 52 weeks, however, the volume did not change significantly with time. Of course, TIBV for the untreated implants was 0 at 52 weeks.

3.2.5. Average bone formation area (Fig. 9)

At 16, 26, and 52 weeks, the average PBFA values for the bioactive implants were 8.4 ± 6.3, 8.5 ± 4.6, 3.4 ± 2.1, and 1.8 ± 1.4, 18.2 ± 10.4, 14.5 ± 9.3, 4.9 ± 4.5, and 3.7 ± 3.6, and 25.0 ± 12.7, 18.7 ± 9.9, 11.8 ± 9.0, and 7.6 ± 7.0, respectively, for p500, p600, p900 and p1200, respectively. The average PBFA in p500 was the greatest at every time point. Hence, the bone formation area was significantly greater in smaller channels at all time points. In

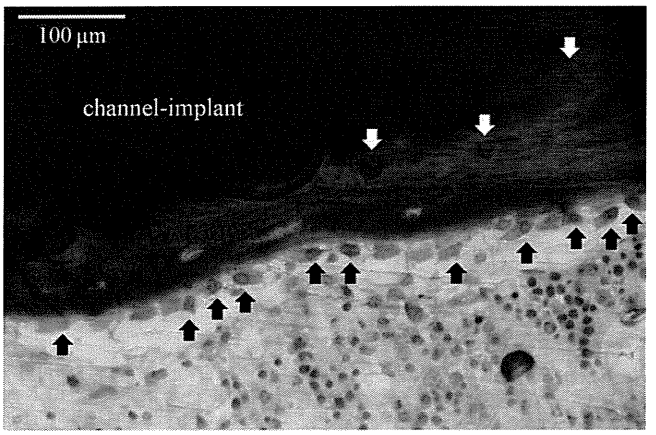

Fig. 5. Magnification of the non-decalcified histological sections 5 mm from the near end of the treated implants at 26 weeks observed by transmitted light microscopy. Obvious bone formation with osteocytes (white arrow) containing blue stained nuclei can be seen. Osteoblast-like cells (black arrow) can be seen as an osteoid-like tissue layer. Stevenel's blue and Van Gieson's picrofuchsin staining. Red color denotes bone.

addition, this tendency for the average bone formation area was similar to that for the bone formation length rate at all time points. The average PBFA for the untreated implant was 0 for all channel sizes at 52 weeks.

3.2.6. Distribution of PBFA

Fig. 10A shows the relationship between PBFA and its location in each channel at 16 weeks. A point 5 mm from the near end represents the peak of the line graph for PBFA in p500 and p600. The line graphs for p900 and p1200 are gentle curves. The peak values of the line graphs for p500 and p600 were higher than those for p900 and p1200.

At 26 weeks the peaks of the line graphs for PBFA in p500 and p600 are somewhat gentle, with a central focus at 5 mm (Fig. 10B). PBFA for p900 and p1200 were high closer to the center of the implants. The peak values of the line graphs for p500 and p600 were higher than those for p900 and p1200, similar to the results for 16 weeks.

At 52 weeks the curves of the line graphs for PBFA are gentler and higher than those at 26 weeks (Fig. 10C). The curves of the line graphs for p500 and p600 were consistently higher than those for p900 and p1200 at 52 weeks.

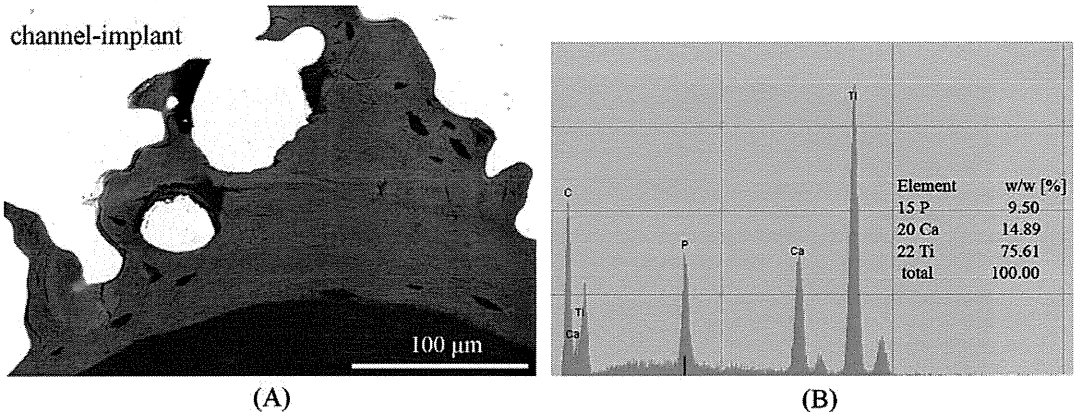

Fig. 6. (A) Backscattered SEM image 5 mm from the near end of the treated implants at 26 weeks. New bone has formed on the channel implant surface and has bonded directly. (B) EDX analysis of the newly formed bone. The bony structure contained calcium and phosphorous; the Ca/P ratio was 1.67 wt.%.

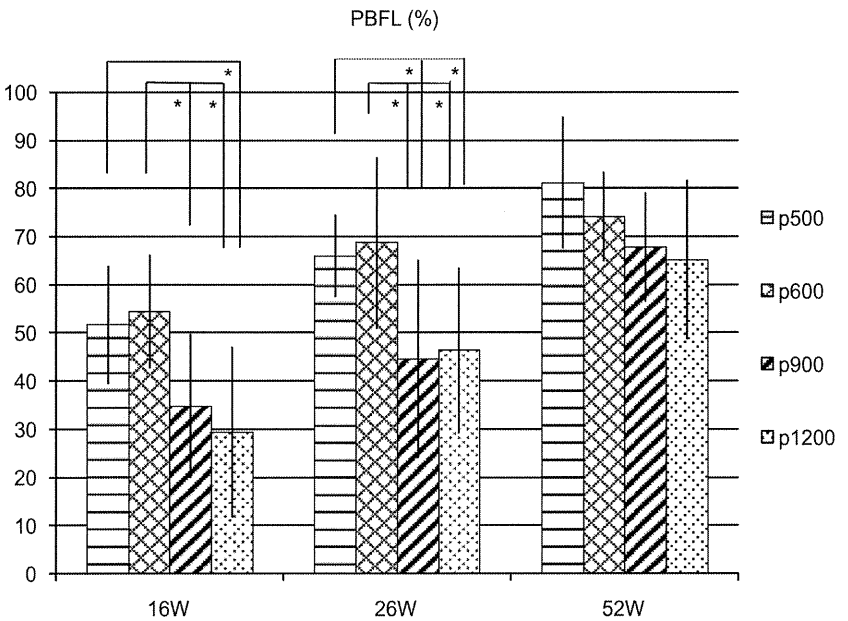

Fig. 7. Histomorphometric results for PBFL at each post-implantation time. In the relatively early post-implantation period PBFL was significantly greater in p500 and p600 than in p900 and p1200. * Denotes significant difference.

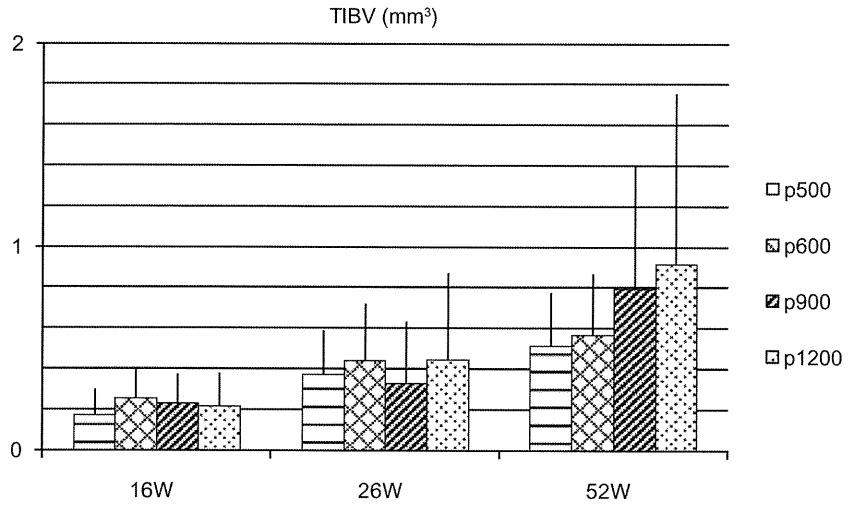

Fig. 8. Histomorphometric results for TIBV at each post-implantation time. As pore size increased TIBV at 52 weeks became greater. However, there was no significant difference for any period ($P < 0.05$).

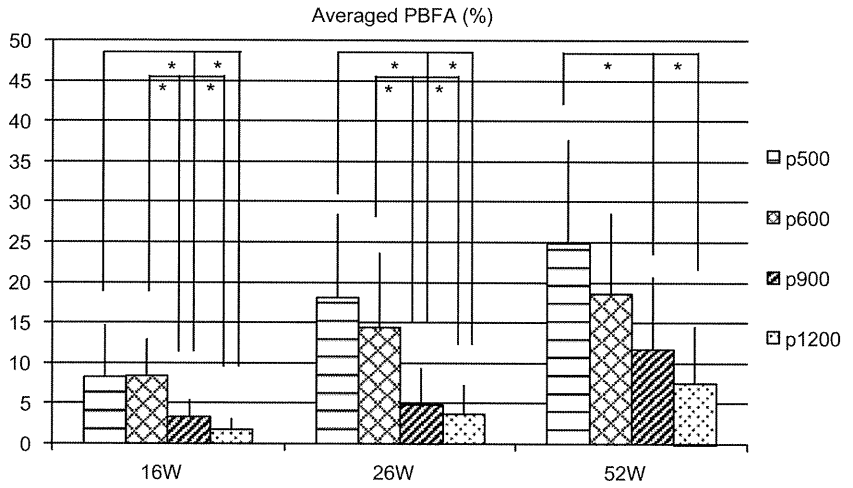

Fig. 9. Histomorphometric results for averaged PBFA at each post-implantation time. Averaged PBFA in p500 was significantly greater than that in p900 or p1200 at all time points ($P < 0.05$). * Denotes significant difference.

4. Discussion

To our knowledge this report presents the first definitive comparison of in vivo osteoinductivity with different interconnective pore sizes (p500, p600, p900, and p1200) of identical implants in identical environments. In addition, we evaluated the location and quantity of bone formed and variations the time-course of formation in each interconnective pore by sectioning each specimen (every 1 mm) after 16, 26, and 52 weeks implantation. These investigations were made possible by the development of our channel implants, whose macrostructure could be controlled by the RP-based SLM technique. Simultaneously, the preparation of homogeneous microstructures and nanostructures by heat treatment at 1300 °C and subsequent chemical and thermal treatment also played an important part in the present experiment. Significant osteoinduction was observed in p500 and p600. Furthermore, we found that the greatest osteoinduction in the early period occurred 5 mm from both ends of the implants in p500 and p600.

A high magnification view of non-decalcified histological sections (Fig. 5) clearly demonstrates obvious bone formation with an osteocyte layer containing blue stained nuclei lined with osteoblast-like cells. When observed by backscattered SEM and analyzed using SEM-EDX it had the structure of lamella bone with osteocytes and had a Ca/P ratio of 1.67. These findings strongly indicate that this bony structure is newly formed bone tissue and not crystal formation or pathological calcification.

Kruyt et al. employed comparative models with different pore sizes and reported that rough HA samples with pores of 800 μm were significantly better than smooth samples having pores of 600 μm with respect to bone formation inside the pores in vivo [32]. Yuan et al. reported that, for almost the same chemical constitution, HA rods with an average pore size of 200 μm and smooth and dense pore walls failed to induce ectopic bone formation, whereas rods with an average pore size of 400 μm and rough and porous pore walls were successful [33]. However, these reports are not accurate comparisons of the pore size because the surface structures of the materials were different. Moreover, it has also been speculated that the degree of interconnectivity of porous scaffolds is more significant than the pore size in the case of vascular networks requiring new bone penetration, and formation is chiefly influenced by the interconnectivity [34]. As a result, simple channel implants such as those in the present study were required to identify the definite effects of interconnective pore size on osteoinduction. The present study has shown that a relationship

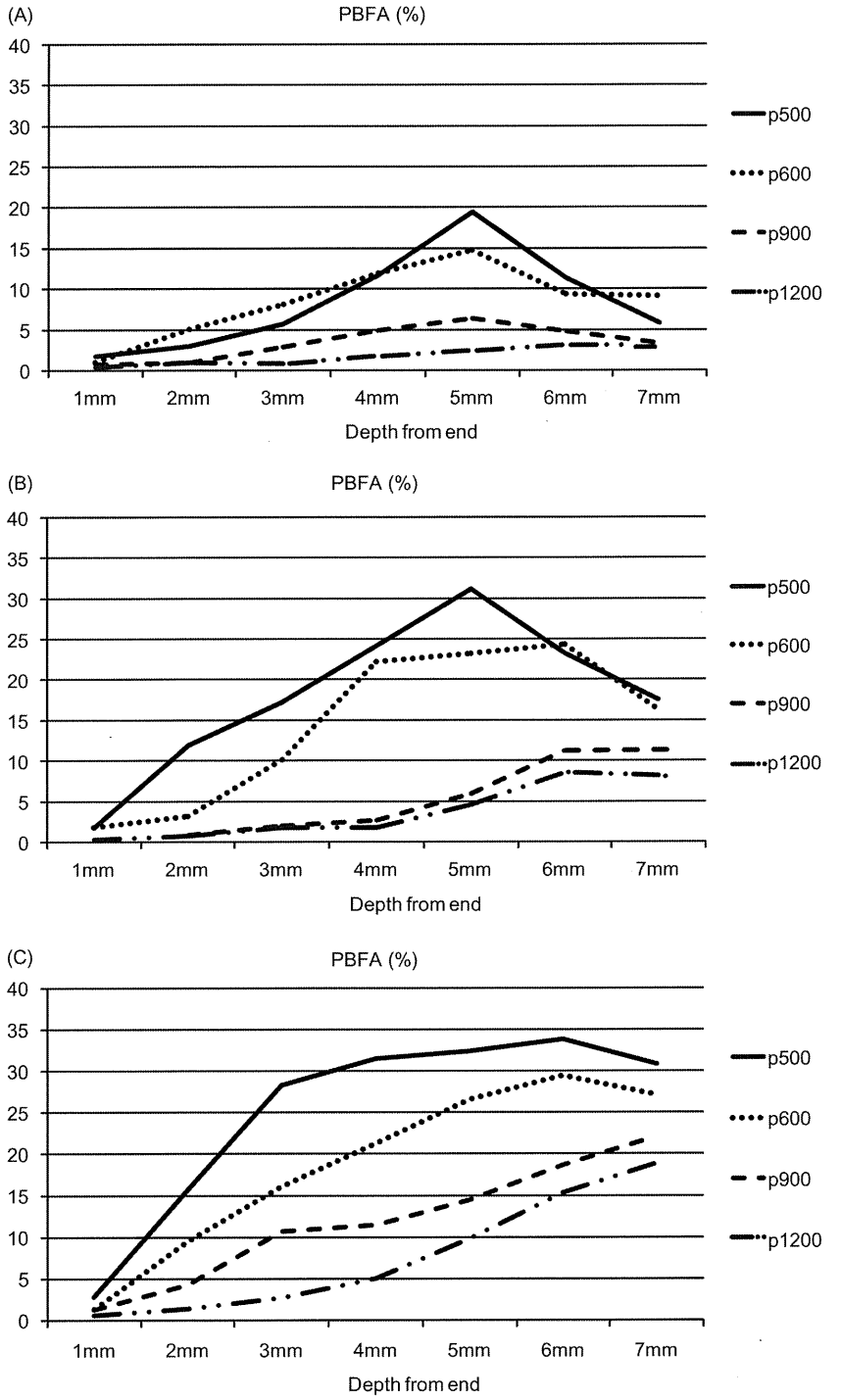

Fig. 10. (A) Location of PBFA of each pore at 16 weeks. A point 5 mm from the near end was the peak of the line graph for PBFA in p500 and p600. Overall, the line graphs in p900 and p1200 formed a low peak. (B) Location of PBFA of each pore at 26 weeks. The peak of the line graph for PBFA in p500 and p600 became gentle with a central focus at 5 mm. (C) Location of PBFA of each pore at 52 weeks. The curve of the line graph of PBFA at 52 weeks became gentler than that at 26 weeks. The peak values for p500 and p600 were higher than those for p900 and p1200 at all locations.

exists between osteoinduction and interconnection size in the range 500–1200 μm.

In terms of the average PBFA, p500 was significantly different from p900 and p1200 at every implantation time point. In terms of PBFL, which is a measure of bone spread, there were significant differences between p500 and both p900 and p1200 and between p600 and both p900 and p1200 at 26 weeks. TIBV showed a tendency to increase with increasing channel size at 52 weeks. However, significant differences were not observed. In general, the fraction of total pore area available for bone formation (average PBFA) is used to evaluate bone formation in the porous body [12,35]. Hence, in studies on porous biomaterials an increase in the ratio of TIBV to total pore volume is a good indicator of improved osteoinductivity. Therefore, of our channel implants we consider p500 (diagonal width 500 μm), which had highest bone area fraction, to be the most osteoinductive, regardless of the implantation period.

In the case of p500 it appears that the concentrations of calcium and phosphate ions could easily reach supersaturation levels, in

contrast to the other channel sizes, because it is smallest. On the other hand, no bone formation could be recognized on the outer surface of the treated channel implants or in any untreated implants at 52 weeks; these results coincide with the consensus that chemical composition, macropores, and poor shear stresses are important for osteoinduction in biomaterials [10,36,37].

In the present study we also evaluated variations in the location, quantity, and time-course of the bone formed in each pore size. These results are represented in terms of the distance from the end (Fig. 10). In the case of p500 and p600 at 16 weeks it appears that osteoinduction might occur at approximately 5 mm from both ends (one-third of the total length). At 26 weeks excellent osteoinduction was observed at distances of 4, 5, and 6 mm from both ends in p500 and p600. We consider that the increasing bone quantity in this region results in it spreading from a point 5 mm distant from both ends. At 52 weeks further excellent osteoinduction was observed at distances of 3–7 mm from both ends of p500. The spread occupied more than two-thirds of the total implant length. In p900 and p1200 the PBFA was better near the implant center than near the ends at 26 weeks, and bone spread was not observed. It appeared that it was particularly difficult for bone formation to spread towards the end of the implant in the large pores. Therefore, we consider that a certain distance from the end is necessary for each pore in accordance with its pore size. In conventional experiments osteoinduction was found to occur only 2.5–3 mm from the implant periphery because the implant itself was 5–6 mm in diameter [8,10,12,35]. In the present study we used channel implants that were 15 mm in length and found that the greatest osteoinduction occurred 5 mm from the periphery in implants with an interconnective pore size of 500–600 μm and at 7 mm from the periphery in pores of size 900–1200 μm. These results suggest that a wider pore throat might be necessary for larger implants.

The mechanism of osteoinduction in porous biomaterials and its biological effects are still largely unknown. However, it has been elucidated that biomaterials must meet very specific requirements in terms of macrostructure, microstructure, and chemical composition in order to be osteoinductive [36]. In terms of macrostructure, Habibovic et al. reported that the pores in interconnected porous structures are an important feature because they provide a protected area without strong fluid movement, thereby giving the cells sufficient space to differentiate along the osteogenic lineage [38]. Our finding that p500 and p600 are more osteoinductive than p900 and p1200 and that in p900 and p1200 osteoinduction occurred deeper in the pores supports their arguments. Besides this physiological theory, the protected pore area in narrow or deep pores has a further advantage with respect to non-susceptibility to myogenic or fibrogenic factors from the surrounding tissue. Kruyt et al. also discussed the importance of a protected pore area for osteoinduction and speculated that the concentrations of calcium and phosphate ions reaches supersaturation levels in the vicinity [37].

In addition, the fact that in p500 and p600 osteoinduction mainly occurred at 5 mm rather than at more distant locations indicates that, to some extent, osteoinduction is influenced by diffusion factors or vascularization or tissue invasion. Kuboki et al. reported that in a bone morphogenetic protein (BMP)-induced osteogenesis model, when blood supply is sufficient such that oxygen and nutrient levels are ample, direct osteogenesis occurred, whereas with lesser vasculature chondrogenesis occurred [39]. In material-induced osteoinduction bone formation is always via direct osteogenesis, indicating that osteoinduction occurs in the presence of a sufficient blood supply; in this respect, peripherals area are more favorable. Thus, as shown in the present study, a distance of 5 mm may represent the optimum balance between vasculature, the availability of calcium and phosphate ions, and fluid movement in the case of p500 and p600. This argument is also consistent with the fact that no bone formation could be seen on the outer surfaces of the treated implants and there was no pore throat occluded by bone anywhere along its length.

For the same reasons, no bone formation could be seen on the outer surfaces of treated p900 and p1200 implants and bone formation tended to occur deeper in the pores. Similarly, there was no pore throat occluded by bone anywhere along its length. These results are consistent with the fact that osteoinduction does not occur in the peripheral pores of a porous implant [12,37].

It appears that the results of the present study represent the initial stages in our understanding of the character and mechanism of osteoinduction in terms of the relationship between osteoinduction and interconnective pore size. Final conclusions can be obtained only by investigating pore sizes smaller than 500 μm and lengths greater than 15 mm. As mentioned previously, the mechanisms responsible for osteoinduction by biomaterials and their biological effects are still largely unknown.

Many reports have discussed the accuracy of reproduction possible with RP techniques [40,41]; the dimensional errors in the present study are approximately identical to values previously reported. However, some issues are still to be resolved, in particular, compared with the design value the measured pore sizes are larger and the outer diameters of the implants are smaller, whereas the implant length is the same. Significant effort is needed to solve these problems and improve precision.

One weakness of the present study concerns only the use of pores wider than 500 μm due to manufacturing limitations. However, we consider that new knowledge has been obtained, as the optimal pore size for osteoinduction has not previously been explored. Investigations of pore sizes less than 500 μm remain a pending issue.

5. Conclusion

The architecture of channel implants whose macrostructure could be controlled by the RP-based SLM technique was very effective for investigating and evaluating the influence of interconnective pore size on osteoinduction. The chemically and heat-treated channel implants exhibited better osteoinductivity and induced ectopic bone growth in the back muscles of beagle dogs within 16 weeks. The resulting bone formation area and length suggested excellent osteoinduction in the case of a 500 μm pore size within the range 500–1200 μm. Furthermore, the highest osteoinduction value in the early periods was observed at a distance of 5 mm from both ends of the implants when the pore size was approximately 500 μm. Further investigations of suitable pore sizes for osteoinduction are necessary for pore sizes less than 500 μm.

Acknowledgements

This work was supported by the Translational Research Promotion Project of the Health Assurance Program of the New Energy and Industrial Technology Development Organization (NEDO).

Appendix A. Figures with essential colour discrimination

Certain figures in this article, particularly Figures 1, 2, 4–6, are difficult to interpret in black and white. The full colour images can be found in the on-line version, at doi: 10.1016/j.actbio.2011.01.036

References

[1] Hench L, Wilson J. Introduction to bioceramics. Singapore: World Scientific; 1993.
[2] Yang Z, Yuan H, Tong W, Zou P, Chen W, Zhang X. Osteogenesis in extraskeletally implanted porous calcium phosphate ceramics: variability among different kinds of animals. Biomaterials 1996;17:2131–7.

[3] Yuan H et al. Bone formation induced by calcium phosphate ceramics in soft tissue of dogs: a comparative study between porous alpha-TCP and beta-TCP. J Mater Sci 2001;12:7–13.
[4] Yuan H, de Bruijn JD, Zhang X, van Blitterswijk CA, de Groot K. Bone induction by porous glass ceramic made from bioglass (45S5). J Biomed Mater Res 2001;58:270–6.
[5] Yamasaki H, Sakai H. Osteogenic response to porous hydroxyapatite ceramics under the skin of dogs. Biomaterials 1992;13:308–12.
[6] Ripamonti U. The morphogenesis of bone in replicas of porous hydroxyapatite obtained from conversion of calcium carbonate exoskeletons of coral. J Bone Joint Surg 1991;73:692–703.
[7] Yuan H, Yang Z, Li Y, Zhang X, De Bruijn JD, De Groot K. Osteoinduction by calcium phosphate biomaterials. J Mater Sci 1998;9:723–6.
[8] Habibovic P et al. Biological performance of uncoated and octacalcium phosphate-coated Ti6Al4V. Biomaterials 2005;26:23–36.
[9] Barrere F et al. Osteogenecity of octacalcium phosphate coatings applied on porous metal implants. J Biomed Mater Res A 2003;66:779–88.
[10] Fujibayashi S, Neo M, Kim HM, Kokubo T, Nakamura T. Osteoinduction of porous bioactive titanium metal. Biomaterials 2004;25:443–50.
[11] Cheng L et al. Osteoinduction of hydroxyapatite/beta-tricalcium phosphate bioceramics in mice with a fractured fibula. Acta Biomater 2010;6:1569–74.
[12] Takemoto M et al. Osteoinductive porous titanium implants: effect of sodium removal by dilute HCl treatment. Biomaterials 2006;27:2682–91.
[13] Habibovic P, Yuan H, van den Doel M, Sees TM, van Blitterswijk CA, de Groot K. Relevance of osteoinductive biomaterials in critical-sized orthotopic defect. J Orthop Res 2006;24:867–76.
[14] Habibovic P, Gbureck U, Doillon CJ, Bassett DC, van Blitterswijk CA, Barralet JE. Osteoconduction and osteoinduction of low-temperature 3D printed bioceramic implants. Biomaterials 2008;29:944–53.
[15] Takemoto M, Fujibayashi S, Akiyama N, Matsushita T, Kokubo T, Nakamura T. Effect of pore structure on osteoconductivity and osteoinductivity of porous bioactive titanium. In: Transactions of the 8th world biomaterials congress. Amsterdam, Netherlands: Curran Associates; 2008.
[16] Habibovic P et al. Comparative in vivo study of six hydroxyapatite-based bone graft substitutes. J Orthop Res 2008;26:1363–70.
[17] Yuan H, van Blitterswijk CA, de Groot K, de Bruijn JD. A comparison of bone formation in biphasic calcium phosphate (BCP) and hydroxyapatite (HA) implanted in muscle and bone of dogs at different time periods. J Biomed Mater Res A 2006;78:139–47.
[18] Ye F et al. A long-term evaluation of osteoinductive HA/beta-TCP ceramics in vivo: 4.5 years study in pigs. J Mater Sci 2007;18:2173–8.
[19] Kondo N et al. Osteoinduction with highly purified beta-tricalcium phosphate in dog dorsal muscles and the proliferation of osteoclasts before heterotopic bone formation. Biomaterials 2006;27:4419–27.
[20] Lin CY, Wirtz T, LaMarca F, Hollister SJ. Structural and mechanical evaluations of a topology optimized titanium interbody fusion cage fabricated by selective laser melting process. J Biomed Mater Res A 2007;83:272–9.
[21] Mullen L, Stamp RC, Fox P, Jones E, Ngo C, Sutcliffe CJ. Selective laser melting: a unit cell approach for the manufacture of porous, titanium, bone in-growth constructs, suitable for orthopedic applications. II. Randomized structures. J Biomed Mater Res B Appl Biomater 2010;92:178–88.
[22] Warnke PH et al. Rapid prototyping: porous titanium alloy scaffolds produced by selective laser melting for bone tissue engineering. Tissue Eng C 2009;15:115–24.
[23] Pattanayak DK, et al. Fabrication of bioactive porous Ti metal with structure similar to human cancellous bone by selective laser melting. In: Sukyoung K, editor. Bioceramics. Daegu; 2009. p. 163–66.
[24] Frosch KH et al. Growth behavior, matrix production, and gene expression of human osteoblasts in defined cylindrical titanium channels. J Biomed Mater Res A 2004;68:325–34.
[25] Karageorgiou V, Kaplan D. Porosity of 3D biomaterial scaffolds and osteogenesis. Biomaterials 2005;26:5474–91.
[26] Ryan G, Pandit A, Apatsidis DP. Fabrication methods of porous metals for use in orthopaedic applications. Biomaterials 2006;27:2651–70.
[27] Scaglione S, Ilengo C, Fato M, Quarto R. Hydroxyapatite-coated polycaprolactone wide mesh as a model of open structure for bone regeneration. Tissue Eng A 2009;15:155–63.
[28] Pattanayak DK et al. Bioactive Ti metal analogous to human cancellous bone: fabrication by selective laser melting and chemical treatments. Acta Biomater 2011;7(3):1398–406.
[29] Kokubo T, Takadama H. How useful is SBF in predicting in vivo bone bioactivity? Biomaterials 2006;27:2907–15.
[30] Kokubo T, Kushitani H, Sakka S. Solutions able to reproduce in vivo surface-structure changes in bioactive glass-ceramic A-W. J Biomed Mater Res 1990;24:721–34.
[31] Maniatopoulos C, Rodriguez A, Deporter DA, Melcher AH. An improved method for preparing histological sections of metallic implants. Int J Oral Maxillofac Implants 1986;1:31–7.
[32] Kruyt MC, Dhert WJ, Oner C, van Blitterswijk CA, Verbout AJ, de Bruijn JD. Optimization of bone–tissue engineering in goats. J Biomed Mater Res B Appl Biomater 2004;69:113–20.
[33] Yuan H, Kurashina K, de Bruijn JD, Li Y, de Groot K, Zhang X. A preliminary study on osteoinduction of two kinds of calcium phosphate ceramics. Biomaterials 1999;20:1799–806.
[34] Zhao J, Guo LY, Yang XB, Weng J. Preparation of bioactive porous HA/PCL composite scaffolds. Appl Surf Sci 2008;255:2942–6.
[35] Takemoto M, Fujibayashi S, Neo M, Suzuki J, Kokubo T, Nakamura T. Mechanical properties and osteoconductivity of porous bioactive titanium. Biomaterials 2005;26:6014–23.
[36] Habibovic P, de Groot K. Osteoinductive biomaterials – properties and relevance in bone repair. J Tissue Eng Regen Med 2007;1:25–32.
[37] Kruyt MC et al. Optimization of bone tissue engineering in goats: a peroperative seeding method using cryopreserved cells and localized bone formation in calcium phosphate scaffolds. Transplantation 2004;77:359–65.
[38] Habibovic P, van der Valk CM, van Blitterswijk CA, De Groot K, Meijer G. Influence of octacalcium phosphate coating on osteoinductive properties of biomaterials. J Mater Sci 2004;15:373–80.
[39] Kuboki Y, Jin Q, Takita H. Geometry of carriers controlling phenotypic expression in BMP-induced osteogenesis and chondrogenesis. J Bone Joint Surg 2001;83A(Suppl. 1):S105–15.
[40] Silva DN, Gerhardt de Oliveira M, Meurer E, Meurer MI, Lopes da Silva JV, Santa-Barbara A. Dimensional error in selective laser sintering and 3D-printing of models for craniomaxillary anatomy reconstruction. J Craniomaxillofac Surg 2008;36:443–9.
[41] Ibrahim D et al. Dimensional error of selective laser sintering, three-dimensional printing and PolyJet models in the reproduction of mandibular anatomy. J Craniomaxillofac Surg 2009;37:167–73.

Acta Biomaterialia 7 (2011) 1379–1386

Contents lists available at ScienceDirect

Acta Biomaterialia

journal homepage: www.elsevier.com/locate/actabiomat

Bone bonding bioactivity of Ti metal and Ti–Zr–Nb–Ta alloys with Ca ions incorporated on their surfaces by simple chemical and heat treatments

A. Fukuda [a,*], M. Takemoto [a], T. Saito [a], S. Fujibayashi [a], M. Neo [a], S. Yamaguchi [b], T. Kizuki [b], T. Matsushita [b], M. Niinomi [c], T. Kokubo [b], T. Nakamura [a]

[a] Department of Orthopaedic Surgery, Graduate School of Medicine, Kyoto University, Shogoin, Kawahara-cho 54, Sakyo-ku, Kyoto 606-8507, Japan
[b] Department of Biomedical Sciences, College of Life and Health Sciences, Chubu University, 1200 Matsumoto-cho, Kasugai, Aichi 487-8501, Japan
[c] Department of Biomaterials Science, Institute for Materials Research, Tohoku University, 2-1-1 Katahira, Aoba-ku, Sendai 980-8577, Japan

ARTICLE INFO

Article history:
Received 2 July 2010
Received in revised form 17 September 2010
Accepted 20 September 2010
Available online 29 September 2010

Keywords:
Titanium alloy
Bioactive treatment
Apatite
Bone bonding
In vivo

ABSTRACT

Ti15Zr4Nb4Ta and Ti29Nb13Ta4.6Zr, which do not contain the potentially cytotoxic elements V and Al, represent a new generation of alloys with improved corrosion resistance, mechanical properties, and cytocompatibility. Recently it has become possible for the apatite forming ability of these alloys to be ascertained by treatment with alkali, $CaCl_2$, heat, and water (ACaHW). In order to confirm the actual in vivo bioactivity of commercially pure titanium (cp-Ti) and these alloys after subjecting them to ACaHW treatment at different temperatures, the bone bonding strength of implants made from these materials was evaluated. The failure load between implant and bone was measured for treated and untreated plates at 4, 8, 16, and 26 weeks after implantation in rabbit tibia. The untreated implants showed almost no bonding, whereas all treated implants showed successful bonding by 4 weeks, and the failure load subsequently increased with time. This suggests that a simple and economical ACaHW treatment could successfully be used to impart bone bonding bioactivity to Ti metal and Ti–Zr–Nb–Ta alloys in vivo. In particular, implants heat treated at 700 °C exhibited significantly greater bone bonding strength, as well as augmented in vitro apatite formation, in comparison with those treated at 600 °C. Thus, with this improved bioactive treatment process these advantageous Ti–Zr–Nb–Ta alloys can serve as useful candidates for orthopedic devices.

1. Introduction

Titanium (Ti) and its alloys are the most popular materials for orthopedic and dental implants because of their superior biocompatibility, excellent corrosion resistance, and good mechanical properties. However, they are essentially bioinert materials that, after implantation in the living body, are merely encapsulated by fibrous tissue that isolates them from the surrounding tissue. On the other hand, orthopedic load-bearing devices such as total hip prostheses require direct bonding between living bone and the implant. Hence, various methods have been developed to promote bone in-growth and implant fixation for Ti and its alloys [1,2], including physical modification of the implant design, modification of the surface topography, and chemical modification of the material composition and structure. Among these methods, plasma sprayed hydroxyapatite coating is one of the most extensively investigated methods, and its efficiency has been confirmed by many reports [3,4].

In the past decade we have developed a chemical and heat treatment method to produce bioactive Ti [5–7]. This method can be used to create a long-lasting bioactive layer on the surface of Ti and its alloys, allowing bonding with living bone via a spontaneously formed apatite layer. In this method the implants are simply immersed in aqueous solutions before heat treatment, and the bonding effects extend homogeneously throughout the irregular structure of the implant. This method is considered superior to the conventional hydroxyapatite plasma spray method, wherein the coating tends to be applied to the most superficial areas, thereby resulting in uneven and inadequate treatment. This alkali and heat treatment was applied to a porous commercially pure Ti (cp-Ti) surface layer on an artificial hip prosthesis made of a Ti6Al2Nb1Ta alloy, and its effectiveness was confirmed in clinical trials in Japan [8]. In fact, this bioactive artificial hip joint was approved for clinical use in 2007 (AHFIX, Japan Medical Materials Co., Japan).

We have also reported that our chemical and heat treatment is effective for Ti alloys (Ti6Al4V, Ti15Mo5Zr3Al, and Ti6Al2Nb1Ta) [9–11]. However, these Ti alloys contain aluminum (Al) and vanadium (V), which are suspected of being cytotoxic [12–14]. In this

* Corresponding author. Tel.: +81 75 751 3365; fax: +81 75 751 8409.
E-mail address: akinobu@kuhp.kyoto-u.ac.jp (A. Fukuda).

1742-7061/$ - see front matter © 2010 Acta Materialia Inc. Published by Elsevier Ltd. All rights reserved.
doi:10.1016/j.actbio.2010.09.026

context, the new generation of Ti alloys without V and Al [14], such as Ti15Zr4Ta4Nb and Ti29Nb13Ta4.6Zr, offers a promising alternative. Ti15Zr4Ta4Nb has been reported to show much better corrosion resistance, mechanical properties, and cytocompatibility than Ti6Al4V [15]; furthermore, Ti29Nb13Ta4.6Zr has been reported to show a lower Young's modulus and cytotoxicity than Ti6Al4V and the same cytotoxicity as cp-Ti [14,16]. Unfortunately, these new generation Ti alloys cannot be endowed with in vitro apatite forming ability by conventional chemical and heat treatment.

Instead, we recently found that Ti15Zr4Ta4Nb and Ti29Nb13Ta4.6Zr can be endowed with in vitro apatite forming ability by treatment with NaOH, $CaCl_2$, heat, and water (ACaHW). In vitro examination showed faster and greater apatite formation on the obtained calcium-modified titanate surface in simulated body fluid (SBF), with ion concentrations nearly equal to those of human blood plasma [17,18]. In this treatment calcium hydrogen titanate is formed after treatment of the Ti surface with NaOH and $CaCl_2$. Subsequent heat treatment transforms the calcium hydrogen titanate into calcium titanates and rutile [17,19]. The final water treatment causes a remarkable increase in in vitro apatite forming ability on account of the increasing mobility of the Ca^{2+} ions via incorporation of H_3O^+ ions in the calcium titanate [17]. These results lead us to expect superior in vivo bioactivity when the ACaHW treatment is applied [20]. In the present study, to confirm the in vivo bioactivity of ACaHW-treated cp-Ti, Ti15Zr4Ta4Nb, and Ti29Nb13Ta4.6Zr alloys, the biomechanical performance was investigated by histological examination and tensile strength testing using animal models [21].

2. Materials and methods

2.1. Implant preparation

Plates of size $15 \times 10 \times 2$ mm were prepared from cp-Ti (Ti > 99.5 mass%), Ti15Zr4Ta4Nb (Kobe Steel Ltd.; Ti balance, Zr 14.51, Nb 3.83, Ta 3.94, Pd 0.16, O 0.25 mass%), and Ti29Nb13Ta4.6Zr (Institute for Materials Research, Tohoku University; Ti balance, Nb 28.8, Fe 0.03,Ta 11.7, Zr 4.65, O 0.08, N 0.01, C 0.01 mass%). The plates were polished with a No. 400 diamond plate, then washed with acetone, 2-propanol, and ultrapure water in an ultrasonic cleaner for 30 min each, and finally dried at 40 °C. For bioactivation the plates were first soaked in 10 ml of 5 or 1 M aqueous NaOH solution at 60 °C for 24 h (alkali treatment). After removal from the solution they were gently rinsed with ultrapure water for 30 s and dried at 40 °C. The plates were subsequently soaked in 20 ml of 100 mM $CaCl_2$ solution at 40 °C for 24 h ($CaCl_2$ treatment), and then washed and dried in a similar manner. Next, they were heated to 600 °C (ACaH600 W) or 700 °C (ACaH700 W) at a rate of 5 °C min^{-1} in an electrical furnace in air and kept at that temperature for 1 h, followed by natural cooling. After the heat treatment they were soaked in 20 ml of ultrapure water at 80 °C for 24 h, and then washed and dried (water treatment). The concentrations of NaOH and the temperatures used for the heat treatment are listed in Table 1. In the present study we did not use ACaH600W-treated Ti29Nb13Ta4.6Zr because the Ti29Nb13Ta4.6Zr alloy had not showed apatite forming ability in SBF on ACaH600W treatment in a preliminary study. Untreated plates were used as controls in the animal experiments. Thus, a total of eight different types of plates were implanted.

Table 1
Conditions of treatment with $CaCl_2$, heat, and water after treatment with NaOH.

	Concentration of NaOH solution (60 °C 24 h)	Heat treatment temperature (1 h)
cp-Ti	5 mol l^{-1}	600 °C
	5 mol l^{-1}	700 °C
Ti15Zr4Ta4Nb	5 mol l^{-1}	600 °C
	5 mol l^{-1}	700 °C
Ti29Nb13Ta4.6Zr	1 mol l^{-1}	700 °C

2.2. Surface analyses

The surfaces of the treated plates were analyzed by field emission scanning electron microscopy (FE-SEM) (S-4300, Hitachi Co., Tokyo, Japan) equipped with an energy dispersive X-ray (EDX) analyzer (EMAX-7000, Horiba Ltd., Kyoto, Japan). The FE-SEM and EDX analyses were carried out at accelerating voltages of 15 and 5 keV, respectively.

2.3. Apatite formation in SBF

The apatite forming abilities of the treated plates were examined by soaking them in 48 ml of SBF with ion concentrations (Na^+ 142.0, K^+ 5.0, Ca^{2+} 2.5, Mg^{2+} 1.5, Cl^- 147.8, HCO_3^- 4.2, HPO_4^{2-} 1.0, and SO_4^{2-} 0.5 mM) nearly equal to those of human blood plasma at 36.5 °C [22]. After soaking for 1 or 3 days the plates were removed, gently rinsed with ultrapure water for 30 s, and dried at 40 °C. Apatite formation on their surfaces was examined by FE-SEM and EDX.

2.4. Animal study

The plates were conventionally sterilized using ethylene oxide gas and implanted into the metaphyses of the tibiae of mature male Japanese white rabbits weighing 2.8–3.5 kg. The surgical methods used have been described previously [5,10,21,23]. Briefly, the rabbits were anesthetized with an intravenous injection of sodium pentobarbital (0.5 ml kg^{-1}), an intramuscular injection of ketamine hydrochloride (10 mg kg^{-1}), and local administration of a solution of 1% lidocaine. A 3 cm long longitudinal skin incision was made on the medial side of the knee and the fascia and periosteum were incised and retracted to expose the tibial cortex. Using a dental burr, a 16×2 mm^2 hole was made from the medial to the lateral cortex running parallel to the longitudinal axis of the tibial metaphyses, as shown in Fig. 1A. After irrigating the hole with saline, the plates were implanted in the frontal direction, perforating the tibia and protruding from the medial to lateral cortex. The fascia and skin were closed in layers and the same surgical procedures were performed bilaterally.

The animals were housed individually in standard rabbit cages and fed standard rabbit food and water ad libitum. Each rabbit was killed with an overdose of intravenous sodium pentobarbital at 4, 8, 16, and 26 weeks after implantation; a total of 128 rabbits were used (eight plates of each type). The Kyoto University guidelines for animal experiments were observed in this study.

2.5. Measurement of detachment failure load

After death the segments of the proximal tibial metaphyses containing the implanted plates were harvested and prepared for the detachment tests [21]. All samples were kept moist after harvesting. The bone tissue surrounding the plates was carefully removed on both sides and at the ends using a dental burr to remove periosteal bone growth. Traction was applied vertically to the implant surface employing load test equipment (model 1310VRW, Aikoh Engineering Co. Ltd., Nagoya, Japan) at a crosshead speed of 35 mm min^{-1} (Fig. 1B–D). Specially designed hooks held the bone–plate–bone construct. The detachment failure load was measured when the plate detached from the bone. If the plate detached before the test then the failure load was defined as 0 N.

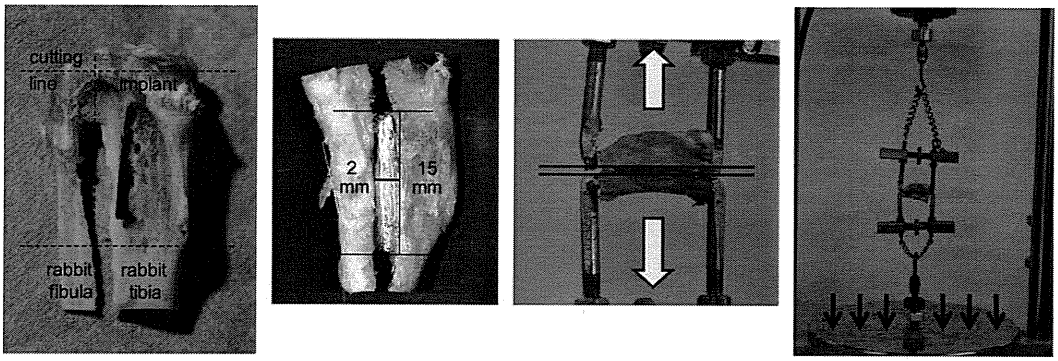

Fig. 1. Photographs of the preparation of rabbit tibia for the detachment test. (A) Insertion of the titanium implant into the tibia (dotted line denotes the cutting line). (B) Detached fragment after cutting the tibia at the proximal and distal ends of the implant. (C) Detachment test. A tensile load is applied by holding the anterior and posterior cortices until detachment. The white arrow indicates the direction of pull. (D) Instron-type autograph. Specially designed hooks held the bone–plate–bone construct. The cross-head speed of the circular disc is 35 mm min^{-1}; the disc moves in the direction of the arrow.

Eight samples were analyzed for each type of implant at each implantation period. All data were recorded as the mean ± standard deviation (SD) and assessed using unpaired one-tailed Student's *t*-test for comparison between untreated and ACaH 700W-treated Ti29Nb13Ta4.6Zr implants at each time point (4, 8, 16, and 26 weeks after implantation), and assessed using one-way analysis of variance (ANOVA) followed by Tukey–Kramer multiple comparison post hoc tests for cp-Ti and Ti15Zr4Ta4Nb at each time point. Differences of $P < 0.05$ were considered statistically significant.

2.6. Histological examination

2.6.1. Surface examination after detachment test

After the detachment tests three samples from each group at each interval after implantation were separated from any soft tissue by soaking in 30% sodium hypochlorite aqueous solution for 3 h. Subsequently they were fixed in 10% phosphate-buffered formalin for 3 days and dehydrated in serial concentrations of ethanol (70, 80, 90, 99, 100, and 100 vol.%) for 1 day each. Then they were soaked in isopentyl acetate solution for 1 day and dried in a critical point drying apparatus (hcp-2, Hitachi Ltd., Tokyo, Japan). The samples were sputter-coated with platinum and palladium for SEM observations (S-4700, Hitachi Ltd., Tokyo, Japan) and coated with carbon for SEM–EDX analyses (EMAX-7000, Horiba Ltd., Kyoto, Japan). The SEM–EDX observations were performed mainly at the sample surface.

2.6.2. Interface examination after detachment test

After the detachment tests five samples from each group at each interval after implantation were fixed in 10% phosphate-buffered formalin for 14 days and dehydrated in serial concentrations of ethanol (70, 80, 90, 99, 100, and 100 vol.%) for 3 days each. Then they were embedded in polyester resin. Sections with thicknesses of 1000 μm were cut using a band saw (BS-3000CP, Exact-Apparatebau, Norderstedt, Germany) positioned perpendicular to the axis of the implant. These sections were polished to a thickness of 30–50 mm using a grinding–sliding machine (Microgrinding MG-4000, Exact-Apparatebau, Norderstedt, Germany) and then stained with Stevenel's blue and Van Gieson's picrofuchsin [24]. A thorough microscopic analysis was performed on histological slides using a transmitted light microscope (model Eclipse 80i, Nikon, Tokyo, Japan) combined with a digital camera (Nikon model DS-5M-L1). Other sections were polished with diamond paper and sputter-coated with carbon for SEM studies.

3. Results

3.1. In vitro evaluation

3.1.1. Surface structures

The EDX results showed that: (1) 3.8–5.3 at.% Na was incorporated on the surface on NaOH treatment; (2) the incorporated Na was completely replaced with Ca on subsequent $CaCl_2$ treatment; (3) the amount of Ca incorporated (4.1–5.9 at.%) remained almost unchanged after subsequent heat and water treatments (3.7–5.2 at.%). Similar tendencies were observed in our previous studies on ACaH600W-treated cp-Ti [19] and Ti15Zr4Nb4Ta [17]. The amount of Ca incorporated did not differ between the ACaH600W- and ACaH700W-treated samples.

Fig. 2 shows FE-SEM photographs of the surfaces of the treated implants. A fine network structure was seen at the nanometer scale on all treated samples, although the alloy plates exhibited a finer network structure than the cp-Ti plate.

3.1.2. Apatite formation

Fig. 3 shows FE-SEM photographs of the surfaces of the treated implants that were soaked in SBF for 1 day. The amount of apatite deposited on the ACaH700W-treated implants increased so that the apatite deposits covered almost the entire surface within 1 day of soaking in SBF. However, the apatite deposits on the surface of the ACaH600W-treated Ti15Zr4Ta4Nb implants only partially covered the surface after 1 day, although they extended to cover the entire surface within 3 days of soaking in SBF.

3.2. In vivo evaluation

All rabbits tolerated the surgical procedure well. None exhibited infection of the surgical site, dislocation of the implants, or adverse reactions such as inflammation or foreign body reactions on or around the implants.

3.2.1. Detachment test (failure load)

Some of the untreated implants were detached from bone prior to testing and were assigned a failure load of 0 N. As seen in Fig. 4, the untreated plates showed a slight increase in failure load throughout the experimental period. In contrast, at all time periods the ACaH700W- and ACaH600W-treated groups both showed significantly higher bonding strength than the untreated groups ($P < 0.001$). Among the cp-Ti and Ti15Zr4Ta4Nb plates the ACaH700W-treated samples showed significantly higher bonding strength than the ACaH600W-treated samples at all time periods.

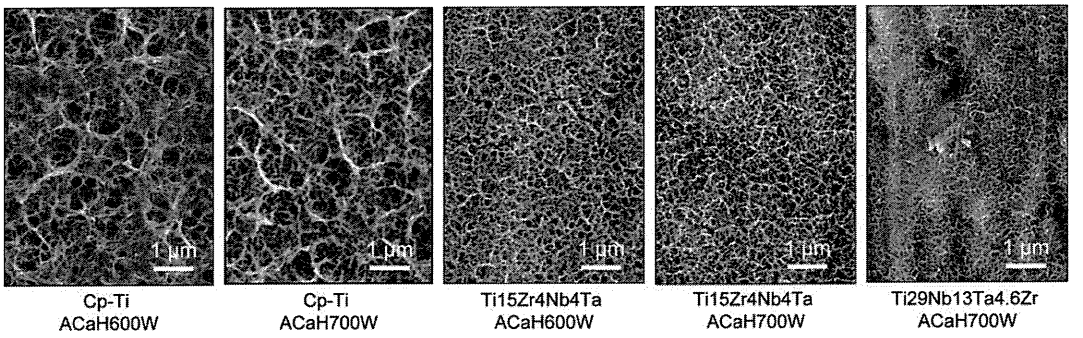

Fig. 2. FE-SEM photographs of the surfaces of the treated implants.

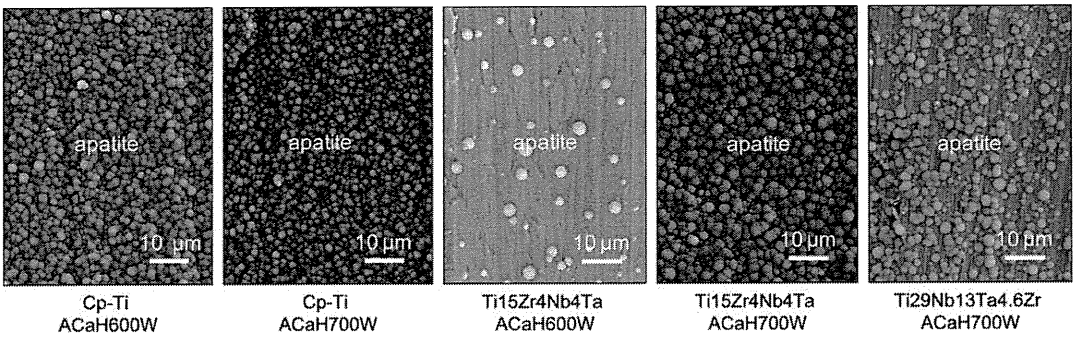

Fig. 3. FE-SEM photographs of the surfaces of the treated implants soaked in SBF for 1 day.

The failure load for all treated groups increased steadily with time. At 4 weeks Ti29Nb13Ta4.6Zr showed a significantly lower bonding strength than cp-Ti and Ti15Zr4Ta4Nb after ACaH700W treatment. Furthermore, from 8 to 26 weeks cp-Ti showed a significantly higher bonding strength than the others after ACaH700W treatment.

3.2.2. Histological examination

3.2.2.1. Surface examination after detachment test. After the detachment tests a bone residue was observed on the intact surface layer of the treated plates in SEM images taken at all time intervals. We could easily distinguish the bony area from the bare metal surface because the average Ca:P ratio in the bony area was 1.66 according to SEM–EDX analysis. In the images taken at 4 weeks there was little bone residue on all untreated plates. In addition, the untreated plates showed almost no increase in bone residue throughout the experimental period. In contrast, some bone residue was observed on the treated plates at 4 weeks, and the amount of residue increased with time. Mature bone was well integrated on the treated plates at all time periods. No significant difference was observed among the ACaH600W- and ACaH700W-treated samples. At 26 weeks, we observed abundant integration of mature bone on the entire treated plate, no surface breakage, and a rupture surface on the bone side for all samples (Fig. 5). Consistent with this finding, in the observations of the bony surface after the detachment testTi was not observed and was not detected by EDX in any sample, indicating that the treated surface structure is sufficiently strong.

3.2.2.2. Interface examination. No inflammatory reactions or adverse effects were observed at the bone–implant interface in all samples subjected to SEM imaging (backscattered mode) and surface staining with Stevenel's blue and Van Gieson's picrofuchsin.

1. At 4 weeks in the untreated group, although immature bone approached the implant, it did not directly bond with the implant, thereby giving rise to a gap between the implant and bone (Fig. 6A). The treated samples, however, all exhibited direct bone–implant bonding, at least partially. However, the bone at the interface was not completely mature in all the implants because of the absence of a laminar structure (Fig. 6). In the stained untreated implant group (Fig. 7A) a little bone formation was found in a transverse direction; the observed bone tissue was of an irregular form without a parallel fibered pattern. In the treated alloy implants newly formed bone bridged the gap, but was coarse and irregular (Fig. 7B, 7C, 7E and 7F). The ACaH700 W-treated cp-Ti implants (Fig. 7D), however, exhibited a bone–Ti interface relatively filled with parallel fibered lamellar bone and bone marrow. Furthermore, the ACaH700W-treated cp-Ti plates had an unclear boundary between new bone and original bone, which indicated bone maturity.
2. At 8 weeks the untreated plates still had a thin layer of intervening fibrous tissue at the interface. However, the treated plates exhibited cortical bone that seemed to extend over the plate. The contact length between cortical bone and implant was wider than that at 4 weeks. Almost complete direct bone bonding was observed in all treated implants.
3. At 16 and 26 weeks the untreated plates still had a thin fibrous tissue layer at the interface or only made partial direct contact with bone (Fig. 8A). Some untreated implants became detached from the bone during cutting, grinding, and staining, which indicated relatively weak bonding. In contrast, the treated samples showed direct bonding with bone and no intervening soft tissue. In particular, the ACaH700W-treated samples exhibited new bone of such maturity that the new bone was undistinguishable from the original bone (Fig. 8D–F), although this was not the case with the ACaH600W-treated plates (Fig. 8B

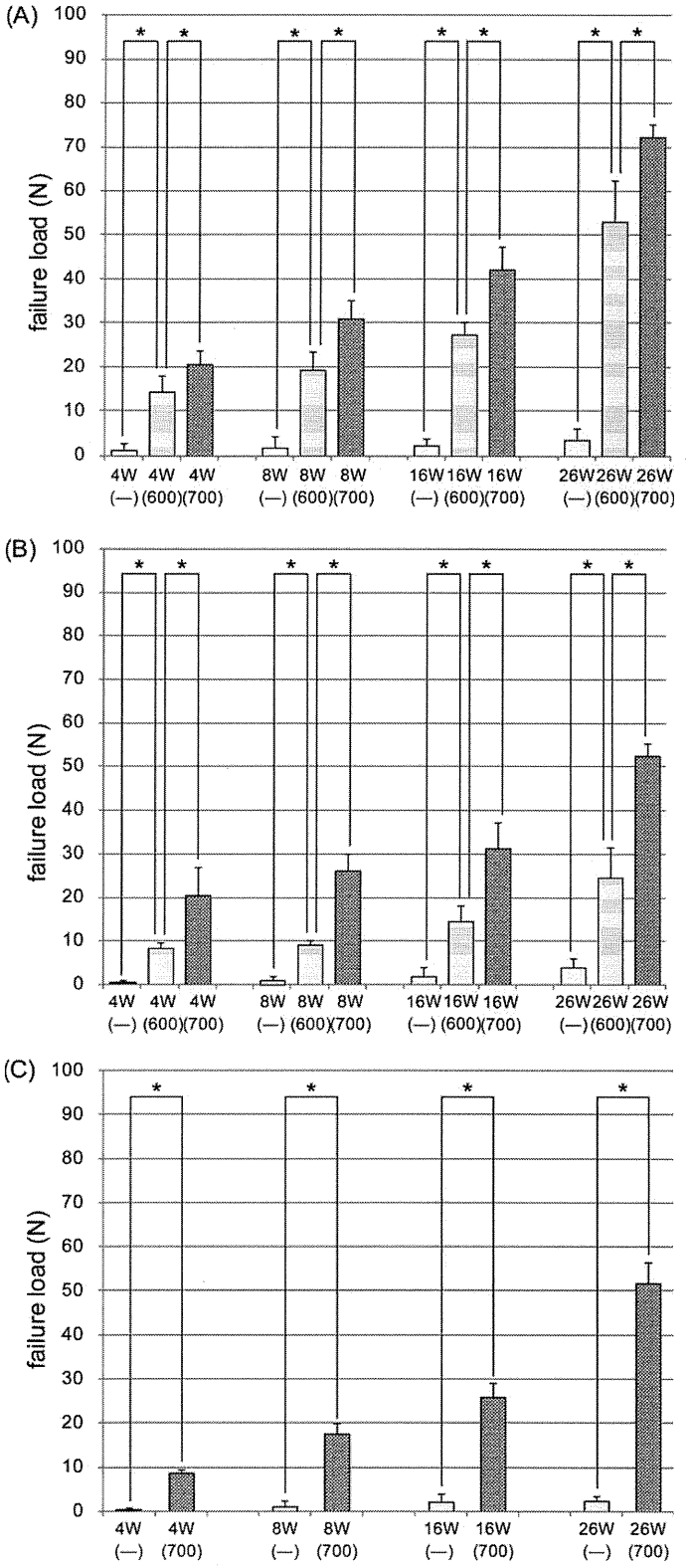

Fig. 4. The results of the detachment test. (A) cp-Ti plates. (B) Ti15Zr4Ta4Nb plates. (C) Ti29Nb13Ta4.6Zr plates. —, Untreated plates; 600, ACaH600W treatment; 700, ACaH700W treatment. The error bars represent standard deviations. * A significant difference.

and 8C). Over time the amount of bone directly bonded to the implant increased, and the directly bonded bone matured and was converted to lamellar bone (Fig. 8B–F).

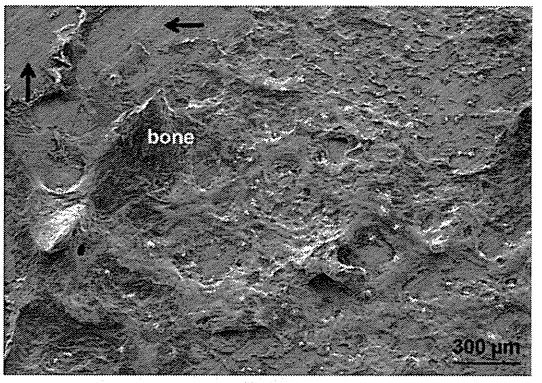

Fig. 5. SEM image of the surface of ACaH700W-treated cp-Ti implants after the detachment test at 26 weeks. Mature bone was well integrated onto the treatment layer. No surface breakage was observed (arrow).

4. Discussion

The results show that all ACaHW-treated implants successfully bonded to bone and retained this bond for up to 26 weeks. In contrast, the untreated implants showed almost no bonding until 8 weeks, and only slight bonding after 16 weeks. Histological examination confirmed that the newly formed bone tissue almost made direct contact with the treated implants as early as 4 weeks after surgery. Conversely, in the untreated implants a layer of fibrous tissue existed at the bone–implant interface 8 weeks after surgery, and bone tissue made only partial contact with the implant at 16 and 26 weeks. These results confirm that ACaHW treatment enhanced bone bonding.

In the present study, cp-Ti showed a relatively higher bonding strength than Ti alloys after ACaHW treatment. The reasons for the differences in bonding strength between ACaHW-treated cp-Ti and Ti alloys are not clear. The bonding strength of the treated substrate is influenced by many factors, such as strength of the substrate and thickness and strength of the treated layers [25]. In general, a thicker calcium titanate layer causes earlier apatite formation and combines with bone earlier than a thin calcium titanate layer. The thickness of the treated layer on cp-Ti and Ti–Zr–Nb–Ta alloys are reported as approximately 1 and 0.5 μm, respectively [17]. This difference may have more impact on the bonding strength than the strength of the substrate.

Ti15Zr4Nb4Ta and Ti29Nb13Ta4.6Zr have been reported to show better biocompatibility than Ti6Al4V [14,16,26,27]. Furthermore, although living bone seems to come close to the surface of these alloys, these bioinert materials do not exhibit osteoconductivity. Recently many researchers have attempted to make these alloys more bioactive, and a few have succeeded [1,2]. Sugino demonstrated apatite formation in vitro on Ti15Zr4Nb4Ta implants subjected to thermal oxidation at 500 °C after machining macrogrooves with widths of 500 μm on the implant surface [1]. Kasuga reported a method for applying a coating of bioactive calcium phosphate invert glass on Ti29Nb13Ta4.6Zr, and showed that the tensile bond between the substrate and coating layer was of high strength [2]. However, these methods cannot be used to treat the entire surface of complex porous implants because of limited apatite formation in the internal surfaces of microgrooves [1] and difficulties encountered with uniform entry of the pulverized glass slurry into the complex microstructure due to its viscous nature [2]. In contrast, our simple method that involves chemical and heat treatment using aqueous solutions and subsequent heat treatment can be used to uniformly treat the entire surface of porous implants having any type of complicated structure. However, our